University of Twente

Master's Thesis

Effects of boundary variations on Rayleigh-Bénard convection

A thesis submitted in fulfilment of the requirements
for the degree of Master of Science

in the

Physics of Fluids Group
Faculty of Science and Technology

Author:
D. Bakhuis

Graduation Committee:
R. Ostilla Mónico, M.Sc.
E.P. van der Poel, M.Sc.
Dr. J.W.J. Verschuur
Assoc. Prof. Dr. C. Sun
Prof. Dr. D. Lohse

UNIVERSITY OF TWENTE

Abstract

Physics of Fluids Group
Faculty of Science and Technology

Master of Science

Effects of boundary variations on Rayleigh-Bénard convection

by D. Bakhuis

In this numerical study, we looked into effects of different boundary variations on the flow dynamics of Rayleigh-Bénard convection. These simulations were done using finite differences on a Cartesian grid for $Ra = 10^6, 10^8$, $Pr = 1, 10$. By adding locally heated spots, so called hot spots, we tried to simulate roughness elements, and possibly position or influence the large scale circulation. For different configurations of these hot spots, we saw no significant effect on the flow dynamics. From this work we saw no observable proof that hot spots can act as surrogate roughness. The next step was to add physical roughness, by using the immersed boundary method. Again, single and even small sets of roughness elements, which were slightly higher than twice the thermal boundary layer thickness, did not influence the large scale circulation in a reproducible way. Placing periodic 1D and 2D wavy patterns had a significant effect on the heat transfer rate of the system. The last part of this thesis focuses on the distribution of equally sized conducting and insulating areas on the top wall boundary and their effect on the flow quantities. When dividing both areas only in two segments, Nu is approximately 2/3 of the homogeneous case. However, by maximizing the number of segments, Nu raises to almost the complete homogeneous case. In a spectral analysis, we showed that the distribution of these areas is indistinguishable outside the thermal boundary layer.

I would like to dedicate this thesis to my loving Kim,
for bringing endless joy to my life.

Contents

CHAPTER 1

Introduction

1.1 Convection

Convection can be described as the motion of fluid which is driven by differential body forces or by surface forces which are acting on the boundary of the fluid. A differential body force can occur if there is a difference in the fluid's density while it is in a gravitational field. This is a well known case and is an example of natural convection. Convection due to surface forces can be induced by a pump or fan which forces the fluid to move. This is an example of forced convection. Most types of convection can by categorized in one of these groups. However, there are other mechanisms possible.

Consider a system which contains a fluid and is heated from below. Due to this heating, the density of the fluid changes locally, resulting in a lighter fluid in the bottom and a heavier fluid on top. This does however not guarantee convective motion. The thermal diffusivity and viscosity of the fluid will try to prevent the onset of this instability. If we induce a large enough temperature gradient between the bottom and top of the system, or in other words, if we heat the system sufficiently, the state becomes unstable and the convective motion becomes visible. This is illustrated in Figure 1.1.

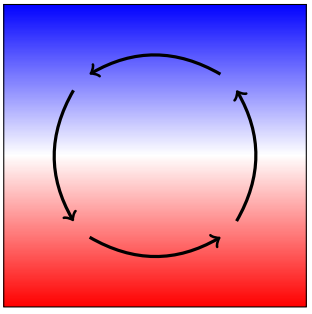

FIGURE 1.1: An example of a system containing a fluid which is heated from below. If the fluid is heated sufficient, convective movement will take place.

In the previous example, fluid was only heated from above, as is often the case when boiling water. This can be problematic as the free surface induces an instability of its own, namely the Bénard-Marangoni convection which is due to gradients in the surface tension, which also come from temperature differences. Therefore, to avoid this, a classical Rayleigh-Bénard setup is often used. This is a confined cell, which is not only heated from below, but also cooled from above.

In 1900, Bénard did the first experiments of this kind [1]. He observed the appearance of hexagonal cells after the onset of the convection. Later, in 1916 Lord Rayleigh showed that the onset of this instability is when the temperature gradient is large enough, and is dependent on a single dimensionless number, the Rayleigh number [2]. This number is defined as:

$$Ra = \frac{g\alpha}{\nu\kappa}\Delta T L^3 \tag{1.1}$$

where g is the gravitational constant, α the thermal expansion coefficient, ν the kinematic viscosity, κ the thermal diffusivity, ΔT the temperature difference between the top and bottom plate, and L is the height of the cell. Lord Rayleigh analytically obtained the critical Rayleigh number for several boundary conditions. For two rigid wall boundaries, he calculated that the onset of convection is at $Ra = 1707$.

1.2 Governing equations

For RB convection, the flow is governed by the conservation equations for mass, momentum and heat. Mass conservation can be preserved by the continuity equation, momentum by the Navier-Stokes equation, and heat by the heat equation. When assuming incompressibility, these equations defined as:

$$\begin{aligned} \nabla \cdot \vec{u} &= 0 \\ \frac{D\vec{u}}{Dt} &= -\frac{1}{\rho}\nabla p + \nabla \cdot (\nu(T)\nabla\vec{u}) + \rho g\hat{x} \\ \frac{DT}{Dt} &= \nabla \cdot (\kappa(T)\nabla T) \end{aligned} \tag{1.2}$$

here we have velocity vector $\vec{u}$, time t, density ρ, kinematic viscosity ν, gravitational constant g, vertical unit vector $\hat{x}$, temperature T, and thermal diffusivity κ.

As Equation 1.2 can be challenging to solve, we use Oberbeck-Boussinesq approximation. This simplifies the equations by stating that density differences are sufficiently small and can be neglected, i.e. the density is kept constant. Only the density variation in the buoyancy term of the equation of motion has to be kept using the following relation: $\Delta\rho = -\alpha\rho_0 (T - T_{ref})$ [3]. Here, the thermal expansion coefficient α is kept constant. This results in dropping the temperature dependence of ν and κ and these quantities can be treated as constants. Density and temperature are assumed to be linearly related. Applying the approximation changes the momentum equation to:

$$\frac{D\vec{u}}{Dt} = -\frac{1}{\rho_0}\nabla p + \nu\nabla^2\vec{u} + \alpha (T - T_{top})\, g\hat{x} \tag{1.3}$$

where ρ_0 is the density at the lower boundary, α the thermal expansion coefficient, and T_{top} the temperature at the top boundary.

Now, the new set of equations will be rewritten in a non-dimensional form. To do this we need to scale all lengths by the height h of the RB system. The time t will be scaled by the free-fall time $t_f = \sqrt{\frac{h}{g\alpha\Delta T}}$, where ΔT is the temperature difference between the top and bottom boundary. All velocities will be scaled by the free-fall velocity $u_f = \sqrt{g\alpha\Delta T h}$. The pressure will be scaled by $\rho_0 u_f^2$. To scale the temperature to its dimensionless form we rewrite it as $\theta = (T - T_{top}) \,/\, (T_{top} - T_{bottom})$, where T_{bottom} is the

temperature at the bottom boundary. Scaling the governing equations results in their dimensionless form:

$$\begin{aligned} \nabla \cdot \vec{u} &= 0 \\ \frac{D\vec{u}}{Dt} &= -\nabla p + \theta \hat{x} + \sqrt{\frac{Pr}{Ra}} \nabla^2 \vec{u} \\ \frac{D\theta}{Dt} &= \frac{1}{\sqrt{RaPr}} \nabla^2 \theta \end{aligned} \tag{1.4}$$

Now the equations have only two dimensionless parameters, the Rayleigh number (Ra) and the Prandtl number (Pr). There are exactly five unknowns to be solved from five equations, which makes this a solvable system of equations.

1.3 Direct numerical simulations

Direct numerical simulation (DNS) is a branch of computational fluid dynamics (CFD) in which turbulent flow problems are solved. When comparing DNS to other CFD techniques, the turbulence is solved explicitly rather than modeled, by for example a Reynolds Averaged Navier Stokes (RANS) closure. Comparing DNS to Large Eddy Simulation (LES), all scales of the flows are resolved. DNS can be seen as an virtual experiment, capturing all the details of the flow at any time of the simulation. Therefore, DNS is ideal for addressing research questions regarding turbulence physics.

DNS, has however also its drawbacks. It is commonly used for three dimensional unsteady turbulent flows, and therefore, time dependent equations have to be solved. To capture all required details, the grid must be fine enough and has to increase when increasing the Reynolds number. The two main drawbacks are the extreme computational costs and a severe limitation in maximum Reynolds number that can be achieved.

There are many different approaches for solving flow problems which all have their own advantages and drawbacks. Examples of these approaches are finite difference, finite volume, and finite element methods. In this study, a matured code is used as a basis which uses the finite difference method [4]. This code has been tested extensively and has proven itself on other research already. A major advantage of the finite difference scheme is that equations can be implemented relatively easy and the constraints for the clustering of points are mild, in comparison with other methods. Also, parallelization of such a solver can be achieved in a relatively straight forward way. This makes it easy to extend the code to the needs of this study.

1.4 Immersed boundary method

One of the most difficult subjects in numerical simulations is flow past or around objects. These objects can be simple spheres, complex aircraft, or special structures attached to the boundary. One method could be to generate a grid around these structures, which is then used to calculate the solution of the flow field. When the objects or structures are moving, this grid has to be revised to fit the new situation and all quantities have to

be interpolated to the new grid. This method is not only costly it terms of CPU time, but the interpolation is also a source of error.

Another method which has the potential to simplify these problems is the immersed boundary method (IBM). Instead of creating a specialized grid around the introduced structures, it solves Navier-Stokes equations on a regular Cartesian grid. The new boundaries are modeled by a new force density which represents the force of the surface boundary acting on the fluid. The force density should be chosen such that the solution of the Navier-Stokes equation satisfies the correct boundary conditions at the surface of the structures. In Equation 1.5 the governing equations have been extended with the extra force density term. Here, $\vec{f}$ is the force density. We have also defined two domains, first the fluid domain Ω_f in which incompressibility is assumed. The second domain is the inside of the immersed structure, Ω_b. At the boundary of this domain with the fluid domain, Γ_b, we assume a no slip boundary condition. Figure 1.2 show a diagram of the situation.

$$\begin{aligned} \rho\left(\frac{\partial \vec{u}}{\partial t} + \vec{u}\cdot\nabla\vec{u}\right) + \nabla P - \mu\Delta\vec{u} &= \vec{f} \\ \nabla\cdot\vec{u} &= 0 \text{ in } \Omega_f \\ \vec{u} &= 0 \text{ on } \Gamma_b \end{aligned} \tag{1.5}$$

In the diagram we see both domains, the white area is the fluid domain Ω_f, and the gray area is the immersed boundary domain Ω_b. A regular Cartesian grid has been placed onto both domains. The circles, filled in black, are the grid points which are immersed. The white circles are the regular grid points in the fluid domain. The surface which splits both domains is the immersed boundary surface Γ_b. On this surface we introduce grid points which are used to calculate the force density $\vec{f}$ induced to the regular fluid grid points. The force density is a function of distance from its originating grid point and will decrease when moving away from the point. The blue dashed circle shows the area of effect of the force originating grom the point. All points that are within this circle "feel" the presence of the boundary. The number of points set on the boundary of the immersed structure depend on the irregularity of the surface. High fluctuations on this surface increases the number of points needed to have sufficient accuracy. The exact function for $\vec{f}$ needs to be modeled in such a way that the solution to Equation 1.5 meet the boundary conditions at the surface of the structure. In this case, it has to meet the no slip boundary condition, $\vec{u} = 0$, at the surface of the immersed surface.

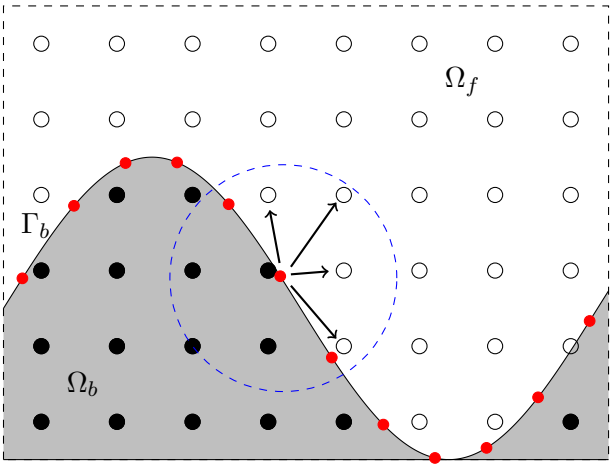

FIGURE 1.2: A example of the IBM used on a wavy boundary. The white area is the fluid, the gray area is the solid boundary, the hollow circles are the regular grid points, the black circles are the immersed grid points. The red dots are the points used to calculate the force density from the boundary surface on nearby grid points. The dashed blue circle shows the area of effect from the boundary point. The black arrows indicate the force density vector from the wall to the nearby grid point.

In case of Rayleigh-Bénard convection we do not only need to take care about the velocities at the boundary, but also of the heat flux. Therefore, a heat flux density, $\vec{q}$, needs to be added to the heat equation part, which enforces the temperature boundary conditions at the immersed boundary.

$$\frac{DT}{Dt} - \kappa \nabla^2 T = \vec{q} \tag{1.6}$$

The advantage of using the IBM is that existing solution techniques can be used. The grid needs no adjustments, only the additional forcing terms need to be computed. Therefore, this method has been added to the existing finite-difference code and extensively tested [5].

1.5 Nusselt number

The Nusselt number is a dimensionless quantity which is a measure for the average heat transfer across the system, normalized by the purely conductive heat transfer. At the boundary, the heat transfer can only be due to conduction, while in the middle of the system, the heat transfer will mainly be due to convection. The definition of the Nusselt number is:

$$Nu = \frac{Q}{\kappa \Delta T h^{-1}} = \frac{1}{\kappa \Delta T h^{-1}} \left(< u_z T >_{x,y,t} - \frac{\partial < T >_{x,y,t}}{\partial z} \right) \tag{1.7}$$

The $\langle \cdot \rangle_{x,y,t}$ denotes the time- and plane average, Q is the total heat transfer. Note that all quantities are dimensional here.

In a short analysis of Equation 1.7 we can check its properties. When looking at the fluid near the no-slip wall, we know that the velocity, u_z is close to zero. Therefore, the heat transfer can mostly be due to conduction, which can also be seen in the equation.

Moving outside of the thermal boundary layer, we have reached 99% of the average bulk temperature. This will result in a very small temperature gradient. The heat transfer will then be mainly due to convection.

One way to calculate Nu is through the volume averaged convection, which is used in this thesis. This definition uses the non-dimensional velocity u_z^* and temperature θ.

$$Nu = 1 + \sqrt{PrRa}\,\langle u_z^* \theta \rangle_{x,y,z,t} \tag{1.8}$$

There are other ways to compute the Nusselt number. For example, close to the wall we are close to the limit of conduction, and the Nusselt number can be found solely by calculating the conduction rate. Another way, is to calculate the heat transfer can be computed from the viscous and heat dissipation rates [6]. As all methods calculate the same quantity, the result should be equal. However, some calculations are impractical or cannot be used. For example, the code used in this thesis can calculate the conduction rate near the walls, but expects them to be flat. Therefore, these results cannot be used.

1.6 Motivation and overview

In this thesis, we will focus on the effect of inhomogeneous boundary conditions on Rayleigh-Bénard (RB) convection. Homogeneous RB has already been studied extensively over the years, see [7, 8] for a recent review on the topic. When looking at experimental work, in almost all cases, a certain degree of inhomogeneity can be found. The boundary always has some microscopic roughness, and heating or cooling is never as homogeneous as desired. This is one of the motivations to study the effect of inhomogeneities on the heat transfer.

One of well known features of a RB system is the Large-Scale Circulation (LSC). The LSC can consist of one or multiple rolls. The boundary layer interacts with these rolls, due to thermal plumes, which are sheared off by the LSC. The LSC is mainly driven by plumes, that are grouped together under the influence of the large-scale horizontal flow near the conducting surface [9]. Several models have been proposed to predict the mean flow structure and its dynamics [10, 11]. It would however be interesting, by introducing additional parameters to control the LSC. For example, by making a small area on the bottom conducting surface slightly hotter, can we influence the position of the thermal plumes or the LSC itself?

First, we will be addressing inhomogeneous temperature boundary conditions in chapter 2. This has already been done by adding a small temperature modulation on the wall boundary [12]. In this study we will be using small areas with locally larger temperature, so called Hot Spots (HS), to add the inhomogeneities. These can also be interpreted as surrogate roughness elements. Using these HS, we investigate the influence on the large scale circulation and the flow dynamics. These HS can have different sizes, intensities, or even be placed as a set of multiple HS. The most ideal configuration needs to be found.

In the next chapter, chapter 3, we will focus on physical roughness. By placing periodic 1D and 2D patterns, their effect on the dynamics of the LSC will be investigated. By adding additional non-flat boundaries, increased plume nucleation has been observed at the protruding edges, which changes the near wall flow dynamics such that there is

increased the heat transfer [13, 14]. Therefore, we will also analyze the heat transfer increase due to these structures. Secondary flow structures have been reported between roughness elements [15]. We will also analyze the flow between the periodic roughness elements.

The final chapter will focus on mixed insulating and conducting boundary conditions only applied on the top wall. By varying the distribution of insulating an conducting patches, and keeping both areas equal, we study the effect on the heat transfer of the system.

CHAPTER 2

Inhomogeneous temperature boundary conditions

2.1 Introduction

2.1.1 General introduction

In this first study we simulate doubly-periodic Rayleigh-Bénard (RB) system in a cubic computational box. This system consist typically of a heated bottom plate and a top plate that is cooled. One of the input parameters is the Rayleigh number, which can be seen as the non-dimensional temperature difference between the top and bottom plate. At a certain Rayleigh number, rolls form in the system and this is the onset of the instability. A roll is a circulation of flow, in this case warmer, less dense fluid moving up and lighter, denser fluid moving down. The position of this roll, which can also be seen as a large scale circulation (LSC), is fixed in time, and appears to be determined purely by initial conditions or numerical noise. The main focus of this study is to add elements to the flow to fix the position of the LSC.

One idea for these elements is to put physical structures in the flow. These structures increase the area locally, which in its turn rises the heat flux locally. We assume that this increase might create a favorable state in which the LSC can position its upward flow. Also the shape of the element might be beneficial for changing the direction of the flow upwards.

The incorporate these elements into the simulation we have to make significant changes to the program by for example hard coding the elements into the grid or using the immersed boundaries technique. Therefore, as an initial project, we focus on simulating these elements by spots on the boundaries which have a higher temperature. These inhomogeneous temperature boundaries can be seen as surrogate roughness. The optimal width and temperature of these spots for fixing the LSC in the system are to be determined by this study.

2.1.2 Program modifications

As we are not physically implementing roughness elements, the modifications to the program can be kept relatively simple. The starting point is the semi-staggered RB program, which has the temperature of each cell not in the center as is the case with a fully staggered grid, but on the cell boundaries of each cell. With the temperature discretized this way, we can set the temperature directly, which is not the case for the fully staggered setup. In Figure 2.1 is a diagram showing the semi-staggered grid.

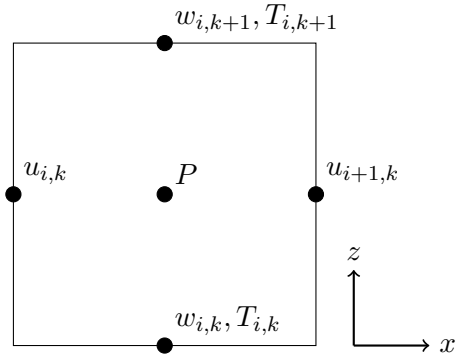

FIGURE 2.1: Location of all the quantities in the simulation cell projected in 2D. The velocity vectors are placed on the borders of the cell and pressure is placed in the cell center. The temperature resides on both, the top and bottom boundary of the cell.

The code has been extended with two new 2D arrays which represent the boundary condition for the top and bottom plate. These can be set by the program internally or read from an external file. The external file is in the HDF5 format and contains the variables, densLowerBC and densUpperBC, which contain the boundary condition values. These can be created with another environment that has better visualization capabilities.

Statistical data is already stored in HDF5 format, however this data is reduced to 1D data by averaging in space. As we want to see the effect in 3D, these routines were extended with 3D statistical routines for all velocities, temperature and convective heat flux.

2.1.3 Geometry and simulation domain

All grids that are used in this study are based on Cartesian coordinates. The grid is uniformly spaced in both horizontal directions. The boundaries in these directions are periodic and therefore no increased resolution is needed at the edges. In the vertical direction the grid is non-uniform. The boundaries are solid plates and increasing the resolution at these borders is beneficial as we can capture more details from the boundary layer. An example of such a grid is shown in Figure 2.2.

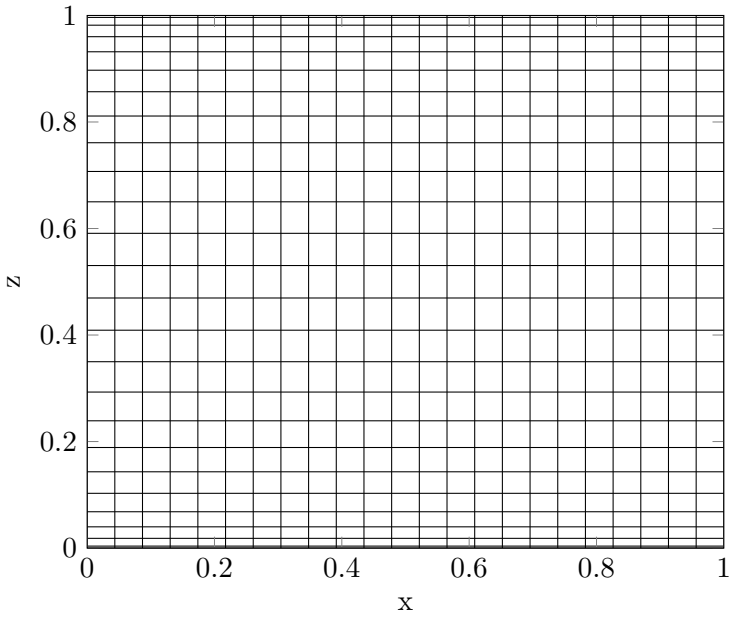

FIGURE 2.2: Example of the non-uniform grid used with a decreasing mesh size at the vertical boundaries.

All simulations that were used for the tests used a grid size of $361 \times 361 \times 289$, however some preliminary tests where done with a grid of $244 \times 244 \times 193$. These grids defined the domain in small simulation cells. As these grids are non-uniform, this result in different minimum and maximum cell size. Table 2.1 shows the different simulation cell dimensions for both grids.

As with all direct numerical simulations all flow scales have to be captured. The large scale circulation needs to be completely in the domain meaning the grid needs to be wide enough. However also the smallest scales needs to be captured which requires the grid to be fine enough. In turbulent thermal convection these scales are the Kolmogorov (η) and the Batchelor (η_θ) scales for the bulk, and the viscous (λ_u) and thermal boundary layer thickness for the plates. To capture these small scales, the grid must be smaller than these quantities. To see if these grids are sufficient, we can approximate $\lambda_\theta/h = 1/(2Nu)$ and $\eta/h = \pi(Pr/(RaNu))^{1/4}$. These results have been calculated for $Ra = 10^6$ and $Ra = 10^8$, and are shown in Table 2.1. These are only approximations for λ_θ and η, however as we are using Prandtl at $\mathcal{O}(1)$, we can assume $\lambda_\theta \approx \lambda_u$, and $\eta \approx \eta_\theta$. Therefore, these scales can be captured with this grid and we can conclude that these grids are sufficient.

Ra	$N_x \times N_y \times N_z$	Δ_{min}/h	Δ_{max}/h	Nu	$\frac{\bar{\lambda}_\theta}{h} = \frac{1}{(2Nu)}$	$\frac{\eta}{h} = \pi\left[\frac{Pr}{(RaNu)}\right]^{1/4}$
10^6	$244 \times 244 \times 193$	2.3×10^{-3}	6.8×10^{-3}	$9.10(\pm 0.41)$	5.3×10^{-2}	1.8×10^{-2}
10^6	$361 \times 361 \times 289$	2.3×10^{-3}	6.8×10^{-3}	$9.34(\pm 0.34)$	5.2×10^{-2}	1.8×10^{-2}
10^8	$244 \times 244 \times 193$	1.1×10^{-3}	4.8×10^{-3}	$32.43(\pm 0.18)$	1.6×10^{-2}	1.3×10^{-2}
10^8	$361 \times 361 \times 289$	1.1×10^{-3}	4.8×10^{-3}	$32.18(\pm 0.17)$	1.6×10^{-2}	1.3×10^{-2}

TABLE 2.1: Simulation cell dimensions due to clustering for two grids and their computed Nusselt numbers for two different Rayleigh numbers. From each Nusselt number the $\bar{\lambda}_\theta/h$ and η/h have been calculated. $Pr = 1$ for all simulations.

The absolute error seen with the Nusselt number, is the statistical convergence error. This error has been calculated by comparing the Nusselt number for half the dataset with the full dataset. All simulations used $Ra = 10^8$ and $Pr = 1$ unless otherwise stated.

2.2 Single hot spot

The first test will use a single spot with increased temperature. To keep the symmetry of the system, the spot will also be placed on the top plate, such that there is a temperature difference of unity. This required for the definition of the Rayleigh number, which is used as an input parameter. The spot itself is preferably continuous, as it otherwise could introduce singularities, therefore, the spot is defined in the following way:

$$H_{spot}(x, y) = \frac{I}{4}\left[1 - \cos\left(\frac{2\pi(x0 - x)}{w}\right)\right]\left[1 - \cos\left(\frac{2\pi(y0 - y)}{w}\right)\right] \tag{2.1}$$

Here, x_0 and y_0 are the coordinates of the spot position, I is the relative intensity of the spot and w is the width of the spot. In Figure 2.3 an example of such a spot is depicted.

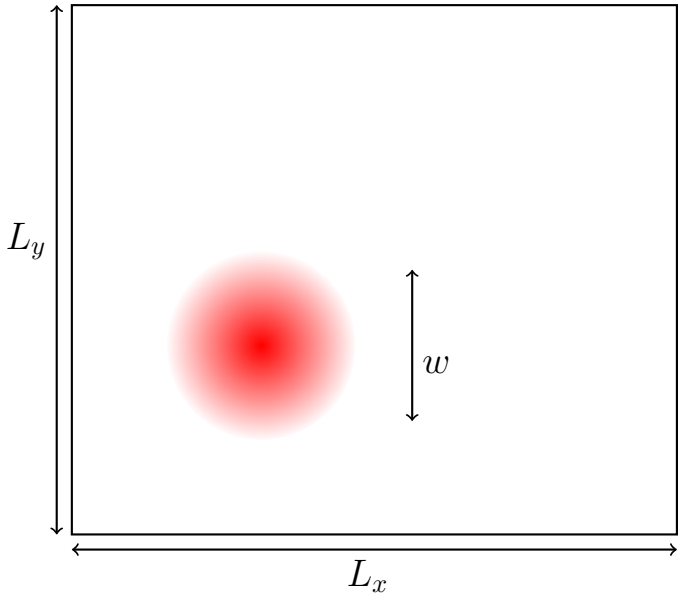

FIGURE 2.3: Spot geometry.

When various parameters for the hot spot are varied, the effect on the LSC has to be monitored. A way to do this is to find the position at which the circulation moves on average upwards. This will be the position at which the temperature of the fluid is on average the hottest and where on average the most plumes are ejected. Now we can calculate the distance between this maximum and the actual position of the hot spot.

2.2.1 Width and intensity variation

In the first test we are going to vary w and I of the hot spot (HS). The position will be fixed for all simulations. All simulations used the same initial simulation as an initial

condition and this will help reduce the transient. The duration for all simulations is set to 100 time units which gave sufficient statistical convergence. As an example, time- and space averaged temperature field plots are shown in Figure 2.4 for two different HS configurations. In this plot, the HS position is indicated by the yellow star. In the flow field, there exists a point in the xy-plane, where on average the flow has the highest vertical velocity. This point, which we will call the HVV point from now on, can be found by finding the maximum in average temperature field. As we want to observe, how this point behaves with respect to the HS, it has been included in the plot by the green star. With the same reasoning, we have a lowest vertical velocity (LVV) point which indicates the point at which the flow field has on average the highest down flow.

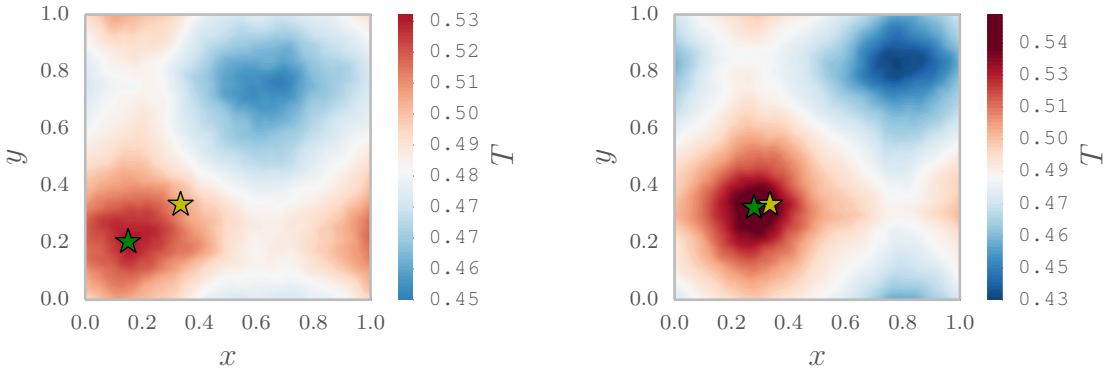

FIGURE 2.4: Time averaged contour plots for the normalized temperature, averaged in the vertical direction. The yellow star is the location of the HS, the green star is maximum temperature which indicates the approximate mean location of the ejecting plumes. The left plot show the result for $w = 0.278$ while the right plot uses $w = 0.417$. Both have $I = 10\%$.

For these simulations all Nu are summarized in Table 2.2. The absolute error for Nu, shown between parenthesis, is expresses as the statistical convergence of the data. This has been done by comparing Nu from the full dataset with Nu calculated from the same dataset, but reduced in length.

Simulation	W (Grid points)	I	Nu
p2t2sa-1	0.139 (50)	10%	33.69($\pm$0.42)
p2t2sa-2	0.278 (100)	10%	34.19($\pm$0.65)
p2t2sa-3	0.417 (150)	10%	33.50($\pm$0.02)
p2t2sa-4	0.278 (100)	5%	33.18($\pm$0.54)
p2t2sa-5	0.278 (100)	20%	34.00($\pm$0.28)
p2t2sa-6	0.278 (100)	30%	33.28($\pm$0.55)

TABLE 2.2: Simulation details and Nusselt number results.

The distances between the HVV, LVV, and the HS have been calculated and are shown in Table 2.3. Except for a spot intensity of 5%, the HS position and the average maximum and minimum temperature position are approximately on a straight line. This might be an indication that a spot intensity of 5% is not sufficient to have any effect.

Hot spot	Distance HS to HVV	Distance HS to LVV	Distance LVV to HVV
W50T10	0.20	0.58	0.65
W100T10	0.23	0.54	0.65
W150T10	0.06	0.65	0.70
W100T5	0.17	0.58	0.68
W100T20	0.15	0.56	0.68
W100T30	0.09	0.46	0.55

TABLE 2.3: Distances between the HVV, LVV, and the HS for all simulations.

Another thing to notice is that the distance between the HVV and the LVV point is more or less constant. As the system uses periodic boundary conditions in the horizontal directions, there is a maximum separation between the HVV and the LVV point, which is $\sqrt{2} \approx 0.707$.

Both, $w = 0.417$ and $I = 30\%$ simulations, have the distance between HVV and HS below 0.1. It is unexpected that the HVV is not exactly on top of the HS. The w and I are relatively large when comparing those to the complete domain. HS could be positioned randomly by the system and it could be coincidence that these HVV are close to the HS. Therefore, we have tested if the $w = 0.417$ is reproducible. All simulation parameters will be equal, except the position of the HS. The results are shown in Figure 2.5.

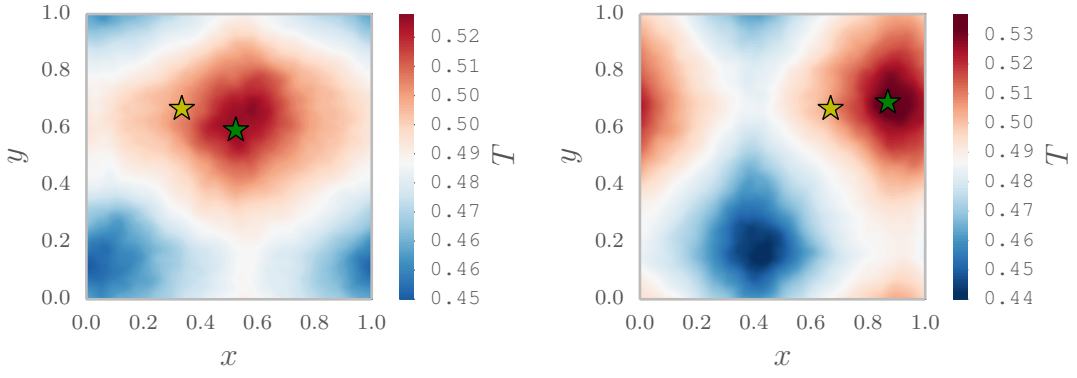

(A) Hot spot at North West corner.

(B) Hot spot at North East corner.

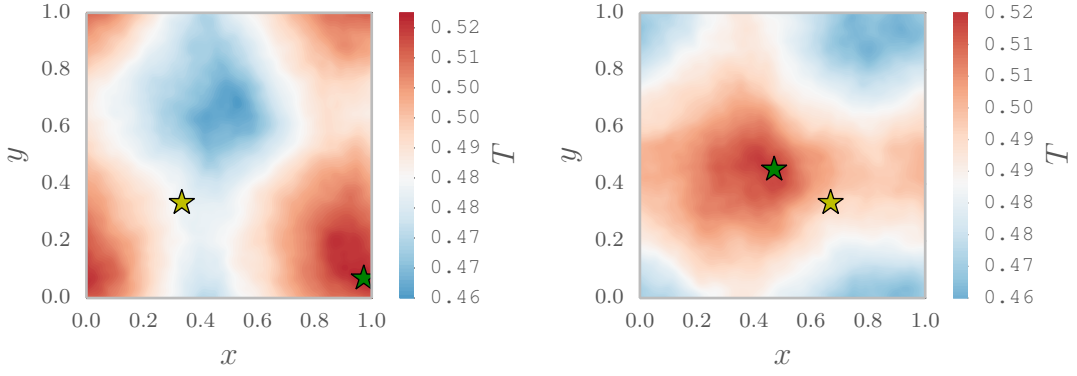

(C) Hot spot at South West corner.

(D) Hot spot at South East corner.

FIGURE 2.5: Time averaged contour plot of the normalized temperature, averaged in the vertical direction. The yellow star indicates the HS, the green star is the HVV which indicates the approximate mean location of the ejecting plumes.

The figure clearly indicates that the former result is not reproducible. The HVV has positioned itself randomly in the domain. The distance between the HVV and LVV points seems more or less constant.

2.2.2 Longer simulation time

One of the first questions that arise is if the HVV will converge to the HS position. To test this, the $w = 1, I = 10\%$ simulation has been resumed and the simulation time has been extended to 350 and 550 time units. The time- and spaced averaged temperature plots are shown in Figure 2.6.

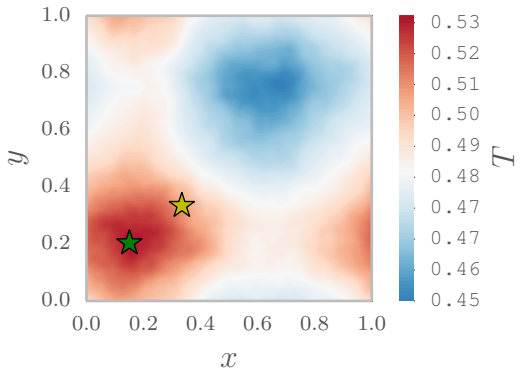

(A) After 100 time units.

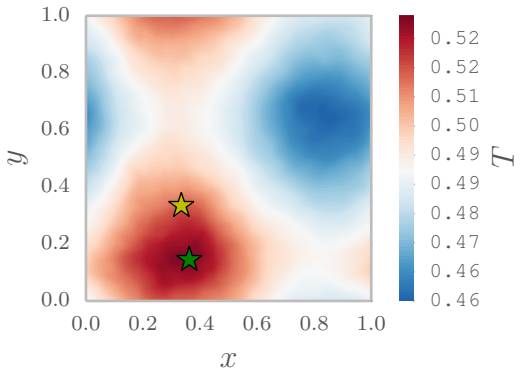

(B) After 350 time units.

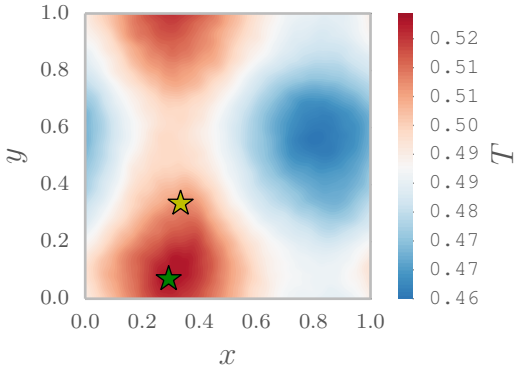

(C) After 550 time units.

FIGURE 2.6: Time averaged contour plot of the normalized temperature, averaged in the vertical direction. The yellow star is the location of the HS, the green star is the location of the HVV.

As can be seen, the HVV point does not move closer to the HS. From these simulations we cannot conclude that the HVV are converging to the HS when increasing the length of the simulation.

2.2.3 Increased Prandtl number

Until now we have not found a HS configuration to place the HVV exactly on top of the HS.

The Prandtl number is a dimensionless ratio for the momentum diffusivity over the thermal diffusivity. This number can be seen as a fluid property as it is only dependent on the type of fluid and its state. In all prior simulations, $Pr = 1$. By increasing this number a factor ten, the momentum diffusivity will be dominant and therefore we expect an increase in mobility of the roll.

This single simulation has $w = 0.278$ and $I = 10\%$ and was run for 200 time units. To cut the transient, the first 50 time units were removed. The Nusselt number for this simulation was $34.15(\pm 0.12)$. The time- and space averaged temperature plot is depicted in Figure 2.7.

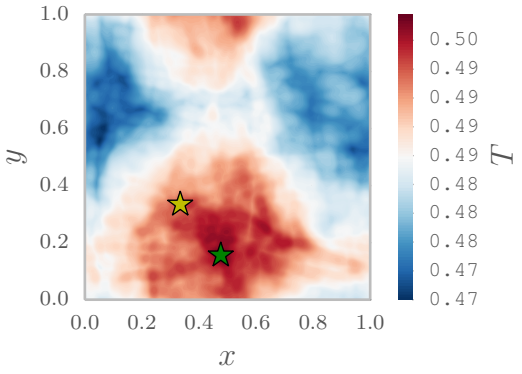

FIGURE 2.7: Time averaged contour plot of the normalized temperature, averaged in the vertical direction, only taking points outside the boundary layer into account. The yellow star is the location of the HS, the green star is the location of the HVV.

It is quite remarkable that even with $Pr = 10$, the HVV is not directly above the HS. The HVV is very close now, but again not exactly on top of the HS.

2.2.4 Asymmetric hot spot

By placing the HS not only on the bottom plate, but also on the top plate, we kept the symmetry to a certain extent. As we did not find the desired effect of placing the HVV on top of the HS, we have chosen to omit this setting and place the HS only on the bottom plate. Again, we set the $w = 0.278$, but now we set $I = 20\%$.

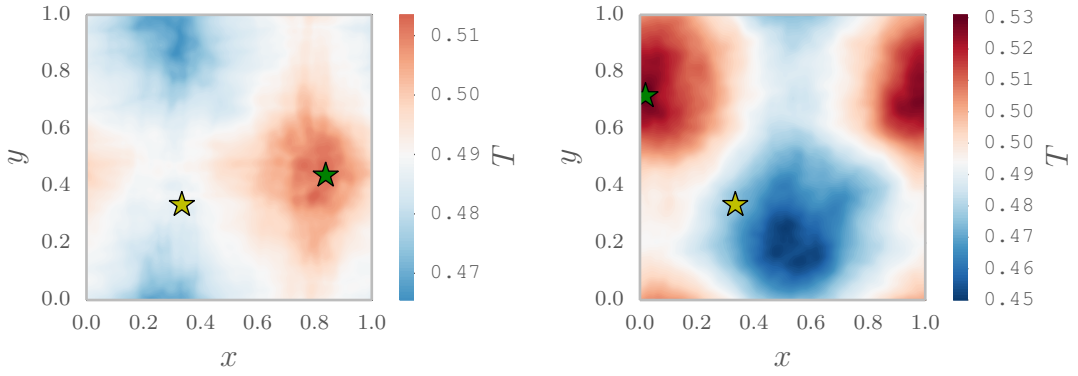

(A) $Pr = 1$, $Nu = 34.31(\pm 0.38)$ (B) $Pr = 10$, $Nu = 34.36(\pm 0.24)$

FIGURE 2.8: Time averaged contour plot of the normalized temperature, averaged in the vertical direction. The yellow star is the location of the HS, the green star is the location of the HVV.

The postion of both, the HVV and the LVV, seem completely random. Until now we have seen no significant effect of the HS on the HVV, nor the LVV. For these asymmetric simulations, Nu is slightly higher when comparing this with the symmetric simulations. When we look at the definition of Ra we see a linear dependence for the temperature difference of the plates. Due to this asymmetric hot spot placement, we slightly increase this difference and therefore, slightly increase Ra. This could be an explanation for the Nu increase.

2.2.5 Crossing stripes

In the previous simulations the temperature inhomogeneities were created using spots. These spots are limited in size and therefore, it might be interesting to increase such a spot in a single dimension creating a stripe. Especially, as we have often seen a stripe-like shape in the HVV and a stripe-like HS might be favorable for positioning the LSC. To include the temperature stripe we will keep its sinusoidal shape in one direction. In these simulations we placed two of such stripes, one in both horizontal directions, which cross each other on a certain position. Two different crossing positions have been simulated. As an additional test, both simulations have been tested with symmetric (on both plates) and asymmetric (only on bottom plate) boundary conditions. These simulation are all done with $Ra = 10^8$ and $Pr = 1$, $w = 0.278$ and $I = 10\%$. The results can be seen in Figure 2.9.

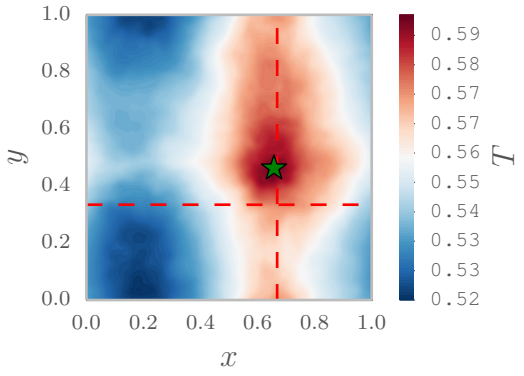

Bottom right, symmetric. $Nu = 32.64 \pm 0.25$.

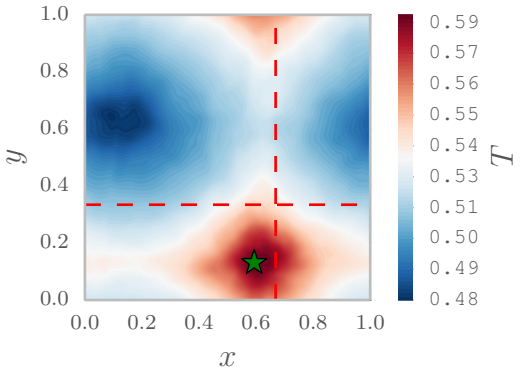

Bottom right, asymmetric. $Nu = 35.20 \pm 0.35$.

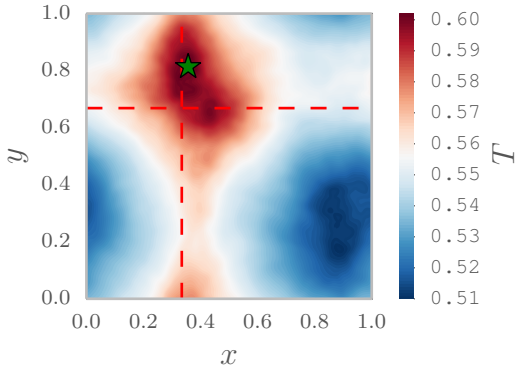

Top left, symmetric. $Nu = 33.44 \pm 0.21$.

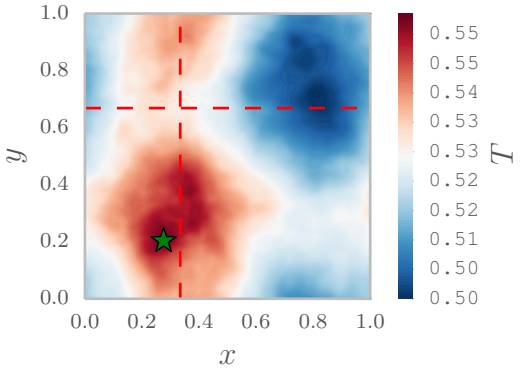

Top left, asymmetric. $Nu = 34.80 \pm 0.03$.

FIGURE 2.9: Time averaged contour plot of the normalized temperature, averaged in the vertical direction. The dashed red lines indicate the center of the inhomogeneous temperature stripes, the green star is the location of the HVV. Note that colors of different plots are not normalized.

The first thing to notice is that the Nusselt number for the asymmetric simulations are slightly higher. Probable reasoning could again be that the temperature difference for the asymmetric case is larger than of the symmetric case, leading to a slightly larger effective Ra. Also, when looking at the stripe-like shapes of the HVV, one of these stripes always seems closely aligned to one of the stripes of the boundary condition. The other, perpendicular stripe, is however not aligned to its counterpart. This results in the HVV not having the center on the crossing of the stripes.

2.2.6 Boundary layer thickness

As we have inhomogeneous temperatures at the boundary, this could have an effect effect on the thermal boundary layer thickness. A thermal boundary layer is a thin layer of fluid, near the vicinity of a wall or object. In this layer the temperature of the fluid changes from the temperature at the wall to the average bulk temperature. It is hard to point an exact position at which the boundary layer ends and the bulk fluid starts. A common definition is the distance from the wall at which the fluid temperature has reached 99% of average bulk temperature. Another definition that is commonly used is

the cross section between the best line fit at the beginning of the temperature profile and the average bulk temperature. This method is sketched in Figure 2.10.

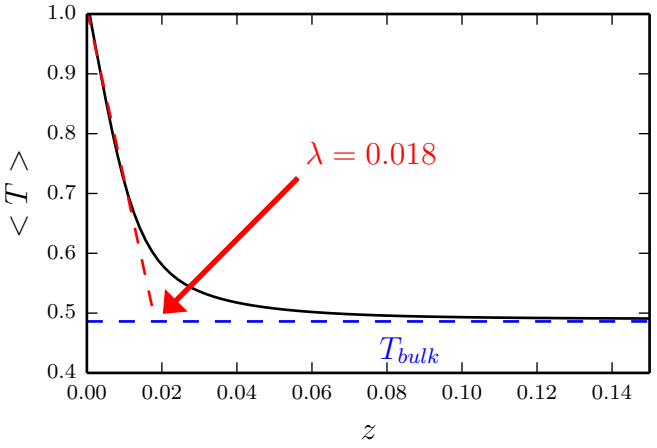

FIGURE 2.10: Time averaged temperature profile near the bottom plate. The red dashed line shows the best line fit for the first part of the temperature profile. The blue dashed line is the average bulk temperature. An approximation for the thermal boundary layer thickness is the cross section between both dashed lines.

Another relation that is often used as an approximation for the thermal boundary layer is $\lambda \approx 1/(2Nu)$. This approximation is identical to the prior line method when assuming an average bulk temperature of 0.5 and is valid for the Ra used in our simulations. When using $Nu = 33$, which is approximately the value for this Rayleigh number, we find an average thermal boundary layer thickness of 0.015.

For the homogeneous RB case, when using the line fitting method, we find $\lambda_{avg} = 0.017$, which is slightly higher. The maximum and minimum are $\lambda_{max} = 0.022$ and $\lambda_{min} = 0.014$. Using the 99% approximation, are a factor five higher and probably incorrect. For this reason, we have chosen to calculate the thermal boundary layer thickness with the line method. For various spot configurations, the thermal boundary layer thicknesses have been approximated in Table 2.4.

Spot	λ_{min}	λ_{max}	λ_{avg}	Spot	λ_{min}	λ_{max}	λ_{avg}
$w = 0.139, h = 10\%$	0.012	0.026	0.017	$w = 0.278, h = 5\%$	0.013	0.024	0.017
$w = 0.278, h = 10\%$	0.012	0.025	0.017	$w = 0.278, h = 20\%$	0.011	0.027	0.017
$w = 0.417, h = 10\%$	0.011	0.025	0.017	$w = 0.278, h = 30\%$	0.013	0.022	0.017

TABLE 2.4: Thermal boundary layer approximations for various HS configurations.

Al result had λ_{min} close to 0.012. Changing any of the spot parameters did not significantly change this value. λ_{max} varied between 0.022 and 0.027. Again, no clear relation could be made between the spot parameters and this approximated value. All λ_{avg} were the same for all spot parameters. This is already an indication that no significant changes in the thermal boundary layer could be observed.

2.3 Onset of decoupling

We have not yet seen a direct coupling between the HS and the HVV. Still, we suspect that if we only have single hot and cold spot, keeping the rest of the plate adiabatic, that the LSC will position itself according to these spots. As an adiabatic wall needs some modification to the code, we can simulate this by setting the plate temperature outside of the HS to the average bulk temperature. These simulation are all done with $Ra = 10^8$ and $Pr = 1$. The spots have $w = 0.278$ and have $T = T_{top} = 1$ for the bottom plate and $T = T_{bottom} = 0$ for the top plate. The spots are now step wise, meaning the spot has a uniform temperature everywhere. This could lead to singularities, but using a gradient would drastically reduce the effect of the spots. The result can be seen in Figure 2.11.

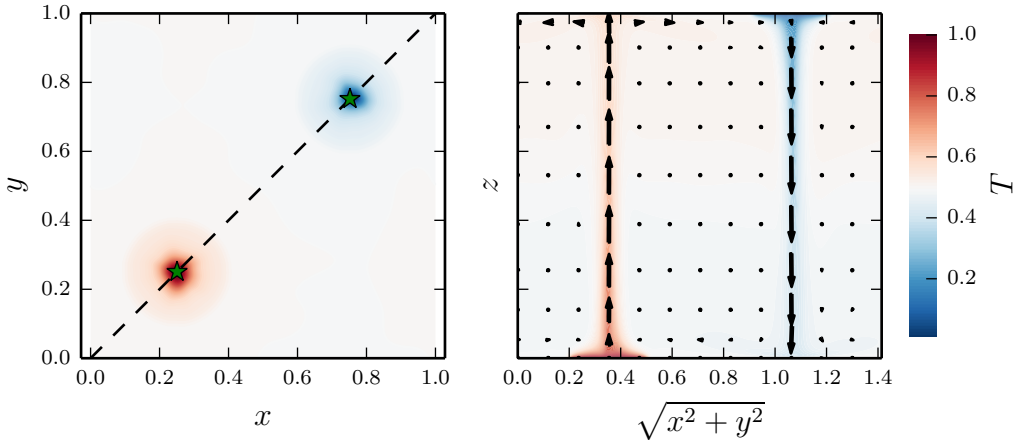

FIGURE 2.11: Left: time- and space averaged temperature plot in the x-y plane. The dashed line indicates the slice which is shown in the right figure. Right: time averaged temperature plot from the dashed line. The arrows show the velocity field. $T_{top} = 0.5$ and $T_{bottom} = 0.5$. The HVV and LVV are exactly on top or below the spots.

As we have only two spots which on average differ with the fluid temperature, the Nusselt number now is only 4.03 ± 0.04. We see clearly that the HVV is positioned exactly on top of the HS and the LVV is directly below the cold spot. Another thing to notice is that the flow narrows down to a relatively thin stream. This stream is only a third in width of the original spot size. It also seems that there is only fluid movement in those streams.

Now we will gradually decrease the difference between the spot and the plate it is on. This will increase the temperature of the bottom plate and decrease the decrease it on the top plate. By decreasing the difference, this will slowly approach the situation we had before. At some point, there should be an onset on which the LSC decouples from the spots.

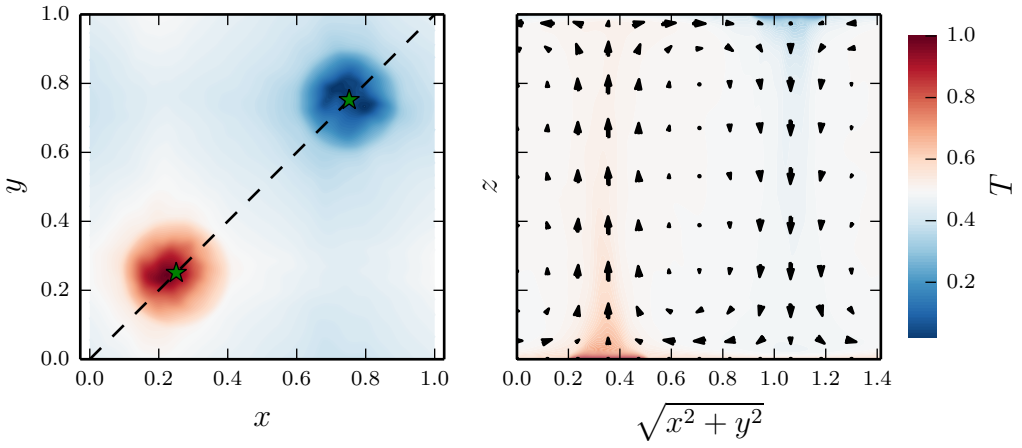

FIGURE 2.12: $T_{top} = 0.4$ and $T_{bottom} = 0.6$. The HVV and LVV are still exactly at the spot. The Nusselt number is increased to 7.58 ± 0.03. The streams are slighly wider and it seems that almost all fluid is moving.

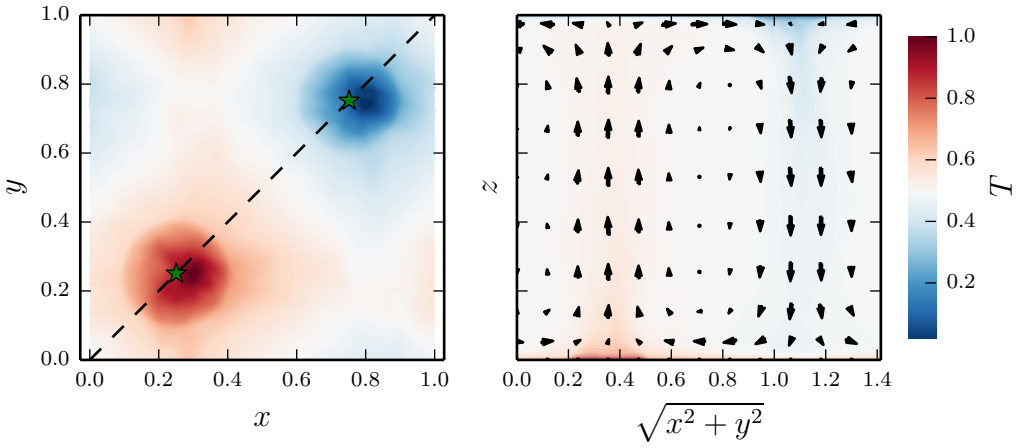

FIGURE 2.13: $T_{top} = 0.3$ and $T_{bottom} = 0.7$. The HVV and LVV are still exactly at the spot. The Nusselt number is again increased to 12.59 ± 0.08. The streams are again slighly wider. The fluid around the hot spot also seems to be affect by the spot.

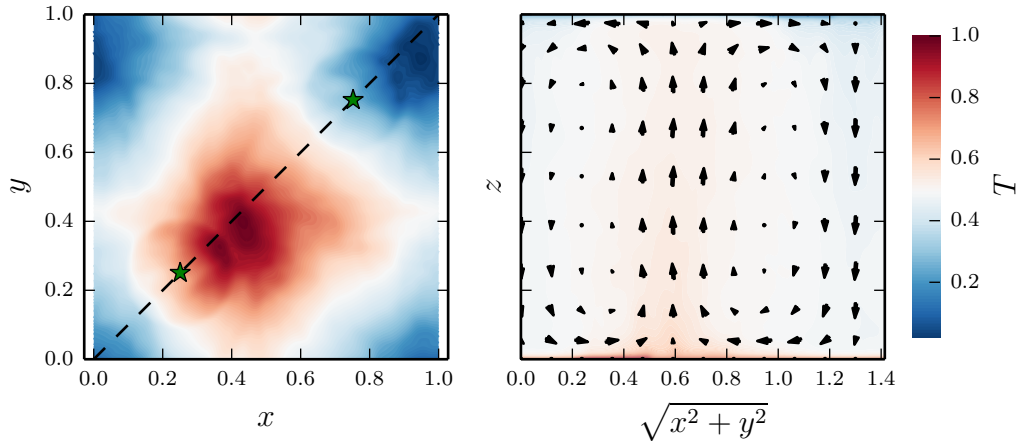

FIGURE 2.14: $T_{top} = 0.2$ and $T_{bottom} = 0.8$. The HVV and LVV are still close but not exactly on top of the spot and this might be around the onset of the decoupling. Both, HVV and LVV seem also larger than the size of the spots. The spots itself are still visible in the left plot. The Nusselt number is now increased to 18.94 ± 0.36.

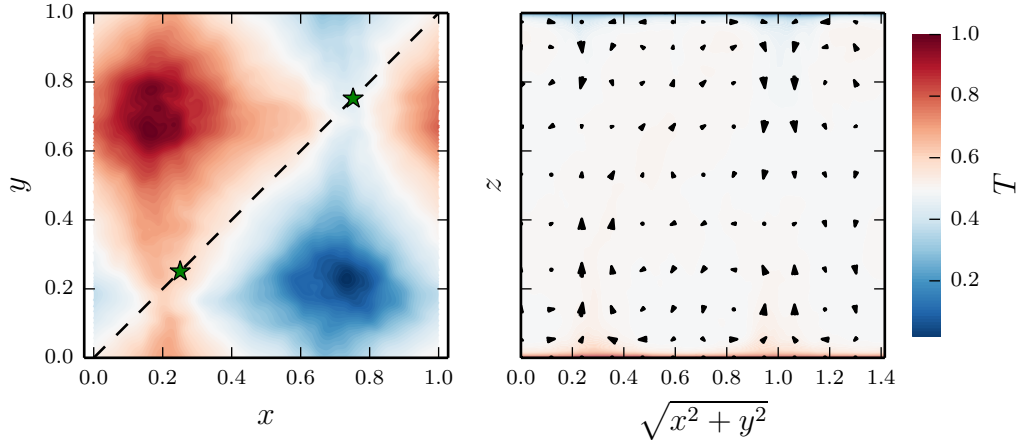

FIGURE 2.15: $T_{top} = 0.1$ and $T_{bottom} = 0.9$. The HVV and LVV are on a complete different position and have lost the coupling with spots. Both spots are not visible anymore in the temperature plot. The Nusselt number for this simulation is 25.01 ± 0.14.

As seen from the prior plots, the decoupling approximately takes place with a temperature difference of around 0.2. If the system is completely decoupled, almost no trace of the spots can be seen in the time- and space averaged temperature plots.

2.4 Multiple hot spots

In the study of single HS, we have tried to find a setting at which the HVV settles itself on top of the HS. Until now we have not yet found this setting. Another interesting question arises if we can break the large scale circulation by adding multiple spots. These HS can again vary in size and intensity, but now also in number. First, we study a set of four HS, which increase in intensity. Thereafter, we use multiple alternating hot and

cold spots. Other variations will be described briefly. These simulation are all done with $Ra = 10^8$ and $Pr = 1$. If not otherwise stated, the spots have $w = 0.278$ and $I = 10\%$.

2.4.1 Increasing hot spot intensity

It this first test we try to break the large scale circulation by positioning four HS into the system and increasing the intensity. The HS will be placed on equal distance from each other, keeping the periodic boundaries in consideration. The intensity of each spot will be increased from 20% to 50% in steps of 10%. The results can be seen in Figure 2.16.

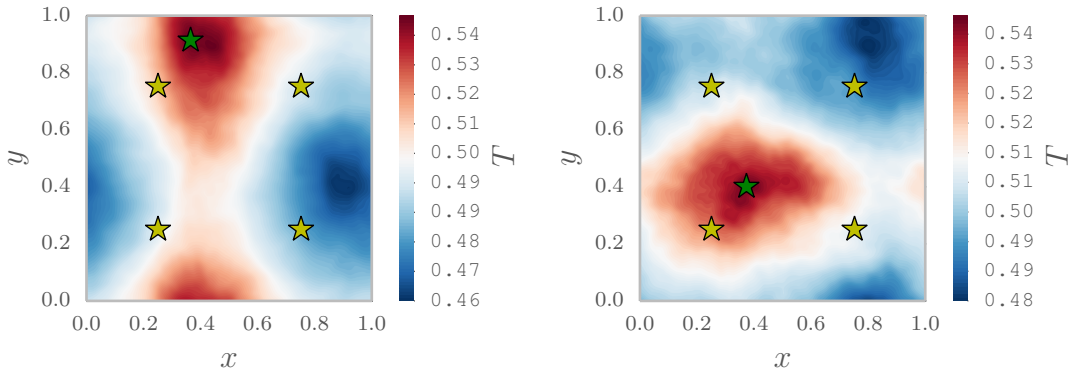

(A) $I = 10\%, Nu = 34.12 \pm 0.09$. (B) $I = 30\%, Nu = 33.67 \pm 0.61$.

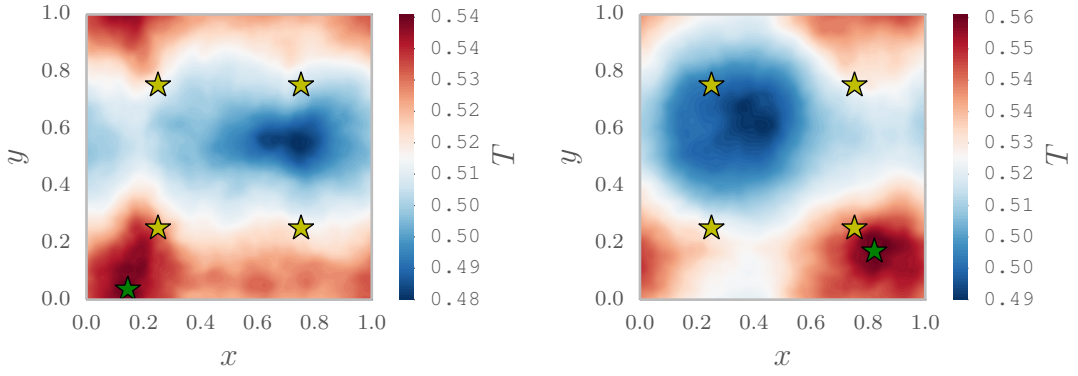

(C) $I = 40\%, Nu = 34.12 \pm 0.45$ (D) $I = 50\%, Nu = 34.21 \pm 0.21$

FIGURE 2.16: Time- and space averaged temperature plot in the x-y plane. The yellow stars are the locations of the HS, the green star is the location of the HVV.

The plots do not show a significant difference with the prior simulations. We also see no break up of the LSC by using these spot settings. All plots show only a single HVV and LVV, which are also seen in, for example Figure 2.6 of the single spot simulations. Some plots have the HVV or LVV extended in a single direction, which gives it a stripe-like fashion. However, the maximum is still visible inside this stripe.

2.4.2 Multiple hot and cold spots

Next, we simulated the system with alternating hot and cold spots. Spots are again placed with equal distance to each other and have $w = 0.278$. The intensity for each

spot is fixed and alternates between $I = 20\%$ and $I = -20\%$. To keep symmetry, the same spots are placed on both, the top and bottom plate. Multiple spots and compositions have been simulated, Figure 2.17 shows only four of them.

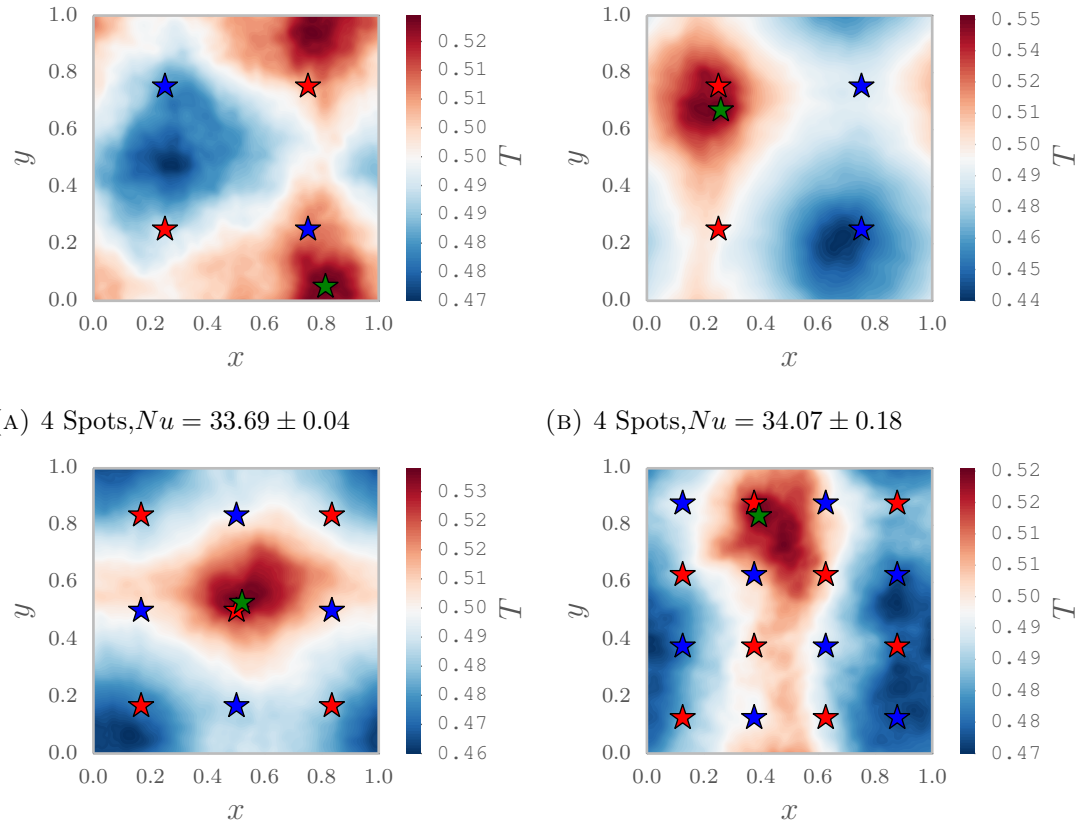

(A) 4 Spots, $Nu = 33.69 \pm 0.04$

(B) 4 Spots, $Nu = 34.07 \pm 0.18$

(C) 9 Spots, $Nu = 33.58 \pm 0.34$

(D) 16 Spots, $Nu = 33.65 \pm 0.05$

FIGURE 2.17: Time- and space averaged temperature plot in the x-y plane. The red stars are the hot spots, blue stars are the cold spots, the green star is the location of the HVV.

Again, all plots are more or less the same with the prior simulations. Only Figure 2.17d does not have a distinct LVV. A break up of the LSC is not visible from these plots. Figure 2.17b has the spots positioned in a symmetric way which seems to strengthen the LSC. From this simulation the average temperature difference between the HVV and the LVV is 0.11, which is the highest recorded.

2.4.3 Other variations

The set of four HS have also been tested in other configurations than varying intensity. Also width variations, position of individual HS, rotation of all four HS, and $Pr = 10$ simulations have been investigated. All of these settings did not break the LSC and gave no additional insights to this study. Therefore, further details are not given for these tests.

2.5 Conclusions

This chapter has studied the effect of inhomogeneous temperatures boundary conditions on the flow dynamics. First, only single spots were placed on the boundaries, with different dimensions and intensities. The idea was to find the spot configuration to position or at least influence the LSC. However, none of the simulations showed a reproducible effect on the bulk flow for any chosen spot width or spot intensity. To ensure that the fixing process is not on a much slower time scale, a single simulation has been extended in length to 550 large-scale turn-over times. This again did not show any significant effect. Also placing the HS only on the bottom boundary did not show any effects on the flow dynamics.

For the same simulations we also looked at the effects of HS on the thermal boundary layer thickness. From these simulations we saw no significant difference in average thermal boundary layers for various configurations of HS. The minimal and maximal thermal boundary layers thickness could not be connected to the different HS parameters.

In a system which has both plates set to the average bulk temperature, except for one hot spot on the bottom and one cold spot on the top. In this simulation, the large scale circulation was perfectly aligned with both spots. After gradually decreasing the temperature difference of each individual plate and the corresponding spot, we have found the onset of the decoupling at a temperature difference of 0.2. When the system is decoupled, almost no trace of the HS can be found in the flow field.

As some final tests, simulation were run with multiple HS and even stripes. These had again no significant effect on the flow dynamics. From all these simulations we could not observe any effect on the LSC. Observing the flow dynamics in the middle of the system did not show any trace of the presence of a HS. This implies that we cannot use a HS to simulate a roughness element.

CHAPTER 3

Physical roughness boundary conditions

3.1 Introduction

3.1.1 General introduction

In the first study we tried to implement artificial roughness by inducing inhomogeneous temperature boundary conditions. As these did not have the desired effect we introduce a new study where physical roughness will be introduced into the system. In a regular RB system the top and bottom boundaries are flat. When using periodic boundary conditions in the horizontal plane, the flow is only restricted in the vertical direction. By introducing roughness, we introduce additional boundaries that do not only restrict the flow in the vertical direction but also in the horizontal direction. Including these additional space parameters, many structures are possible, for example, simple wave-like structures or small cavities. To include these structures, we use the immersed boundary method (IBM). With this method we do not need to change the grid. Due to the immersed boundary we need to two new terms, a force density $\vec{f}$, and a heat flux density $\vec{q}$, to the governing equations. This two terms add the artificial force density and heat flux density as if there was an actual boundary in the fluid and enforce the boundary conditions.

With various structures implemented we want to study the effect on different quantities in the Rayleigh-Bénard system. First, we have a look at some global quantities such as the Nusselt number and the bulk temperature. Also local quantities such as the local temperature on different positions on the structures will be investigated. When varying these different structures, we will also try to find an optimum for the heat transfer. As there are unlimited possibilities for different structures, we will limit the structures to 1D and 2D waves, triangle waves, and single spots.

3.1.2 Program modifications

As a starting point, we use the fully staggered pencil code. This code parallelizes the domain not in horizontal slabs, but in vertical square tubes or pencils and it has already been proven to be very efficient. First, an existing version of the IBM has been merged with this version of the code. The existing extension creates a new file in which the topography of the top and bottom plate can be set. With regular IBM it is possible to have fully immersed structures, however with this code it is only possible to have an elevated boundary from the plate. Additional functions have been written for the different structures used in this report.

As the new code is using a different way to divide the domain, the 3D statistical routines need to be adjusted for this. Again, all velocities, temperature, and the convectie heat flux are stored to a HDF5 file for later analysis.

3.2 Wave patterns

3.2.1 Geometry and simulation domain

The first patterns we are going to analyze are the wave patterns in one and two dimensions. Both patterns are only placed onto the bottom plate. The top plate is kept flat for all simulations. The wave introduced is a sinusoidal wave with a frequency chosen in such a way that the wave length, or a multiple of, is exactly the domain length. The bottom or valley of the sine should not be lower than the bottom of the system. This can easily be achieved by using the amplitude as the base height. The height of the wave should not be to high but at least moderately higher than the boundary layer. As an approximate for the boundary layer height we can use the relation for homogeneous RB, $1/(2Nu)$, which gives us a height of about 0.016. Therefore, an amplitude of 0.025 will be high enough. The peaks of the wave will be at 0.05 with the base at 0.025. The wave pattern in two dimensions will use the same frequency for both directions. The equations used for creating the wave patterns are shown in Equation 3.1. The typical geometry for the 1D and the 2D wave pattern system are shown in Figure 3.1 and Figure 3.2.

$$H(x,y) = B + A\sin(2\pi f x) \qquad x \in (0,1), \forall y, f \in \mathbb{N} \tag{3.1a}$$

$$H(x,y) = B + A\sin(2\pi f x)\sin(2\pi f y) \qquad x \in (0,1), y \in (0,1), f \in \mathbb{N} \tag{3.1b}$$

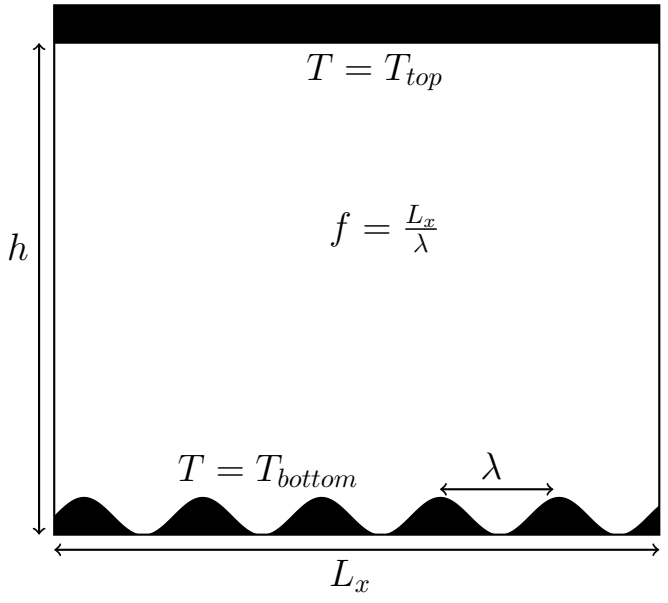

FIGURE 3.1: The 2D projection of geometry used for the physical roughness wave pattern simulations. The structures are only present on the bottom plate which has the temperature set to T_{bottom}. The top plate is flat and has the temperature set to T_{top}. The wave pattern only varies in the x direction and is equal for all y.

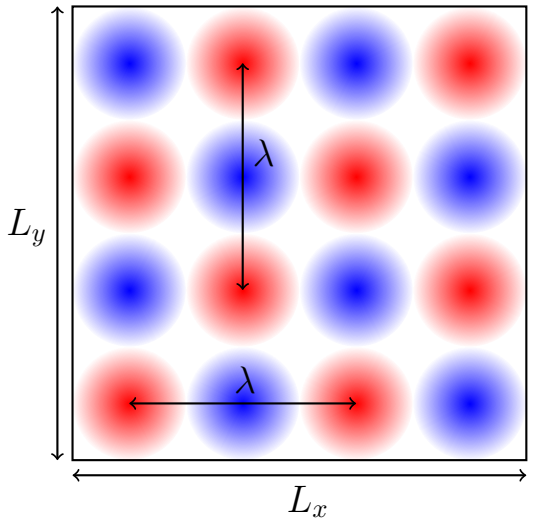

FIGURE 3.2: The 2D projection of geometry used for the physical roughness 2D wave pattern simulations. The wave length λ is the same for both directions. Again, the structures are only present on the bottom plate.

As we are now introducing a wave pattern onto the bottom plate we are effectively increasing the area of that plate. This increase in area will affect the heat transfer as more fluid will be in contact with the new area. The increase in area when compared to a flat plate has been calculated in Table 3.1.

f	A_{wave}	A_{wave2d}	f	A_{wave}	A_{wave2d}
1	0.6%	0.6%	6	19.4%	19.8%
2	2.4%	2.4%	10	46.4%	47.9%
3	5.3%	5.3%	20	130.7%	137.4%
4	9.2%	9.3%	36	280.8%	297.7%

TABLE 3.1: The increase in area when comparing to a flat plate for the 1D and 2D wave pattern for various frequencies.

As for the inhomogeneous temperature simulations, the grid has been set to $361 \times 361 \times 289$, which is fine for $Ra = 10^8$ and $Pr = 1$. The height has been set to unity, however this is only the case exactly in the valley of the wave pattern. At the peak of the wave pattern the distance is only 0.95. Both aspect ratios in the x-, and y-direction are set to 1 which results in a square box.

3.2.2 Flow visualization

To give a feel for the flow fields and how these structures look in the system, snapshots have been created. In Figure 3.3 the instantaneous temperature field for four and twenty waves are shown. Figure 3.4 shows the same temperature field for the 2D wave pattern.

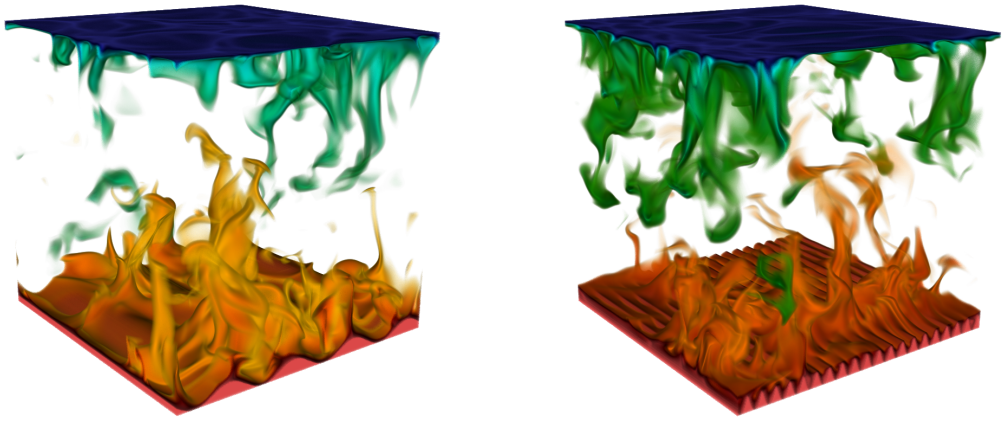

FIGURE 3.3: Snapshot of the instantaneous temperature field for four and twenty wave patterns.

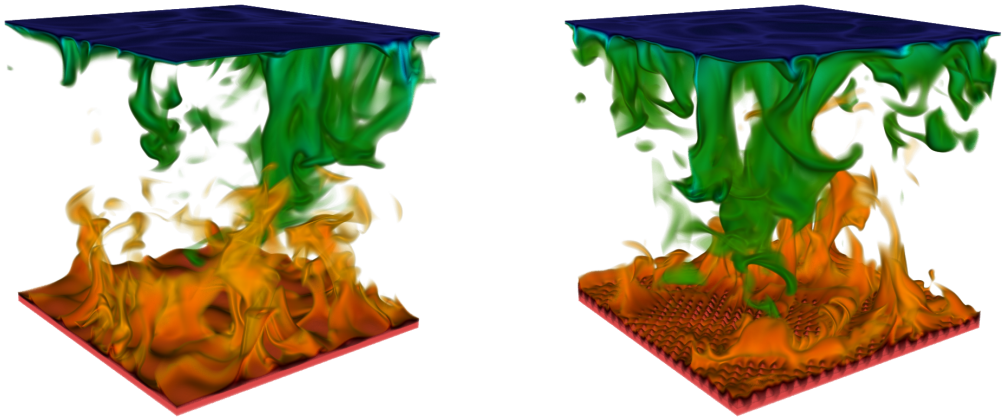

FIGURE 3.4: Snapshot of the instantaneous temperature field for four and twenty 2D wave patterns.

3.2.3 Global quantities

First, we will focus on the effect of the patterns on the heat transfer of the system. Heat is injected from the bottom plate, and is transfered through the fluid to the top plate, at which it can exit the system. In Figure 3.5 the Nusselt number has been plotted in two different ways, the regular Nusselt number in blue and the area compensated Nusselt number in red. Error bars show the statistical convergence of the Nusselt number. When looking at the plane Nusselt number, we see a slight increase with an optimum at the $f = 10$. After the optimum the Nusselt number decreases again. When we look at the velocity field between the wave pattern structures for $f = 6$ we see that the flow is on average downwards in the center of the valley and on average upwards on the sides of the hill. As snapshot of the average velocity profile is shown in Figure 3.6 for a single wave structure, however this can be seen on average for all waves in this simulation.

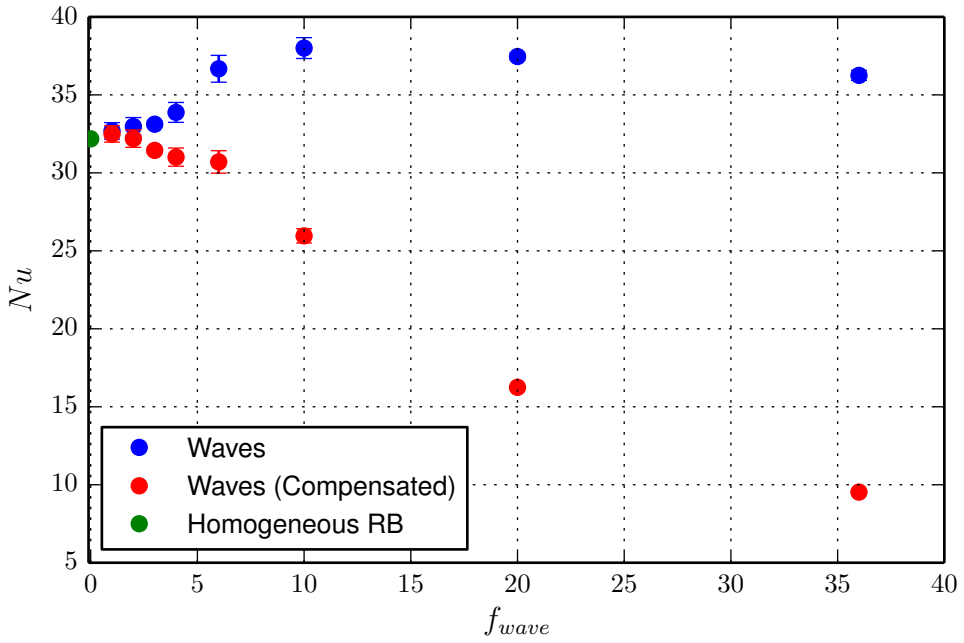

FIGURE 3.5: The Nusselt number is plotted against the frequency of the wave pattern. In blue, the Nusselt number is plotted in its regular way, while in red the same Nusselt number is compensated for the increase in area. In green, at a frequency of zero the homogeneous case has been plotted for reference.

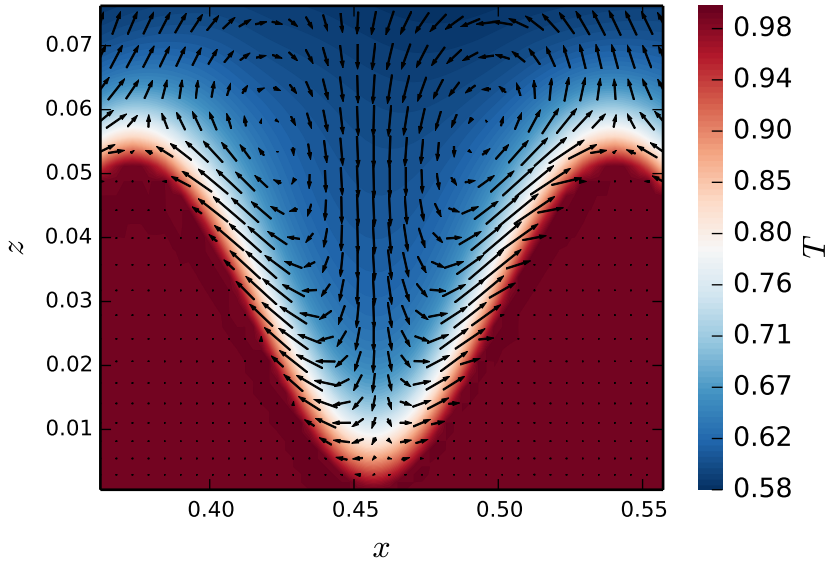

FIGURE 3.6: Detail of the time and space averaged flow field in the cavity of the sinusoidal wave structures. On average the flow is directed downwards at the center of the valley and is directed upwards at the side walls.

When investigating the flow field between the wave pattern of $f = 20$ we see on average two circulations. First the large scale circulation that is moving perpendicular over the wavy structures, which only moves slightly with the shape of the waves. Between the

waves, in the valley of the sinusoidal structures we see a secondary circulation, which resembles a flow in a cavity. This can be seen in Figure 3.7.

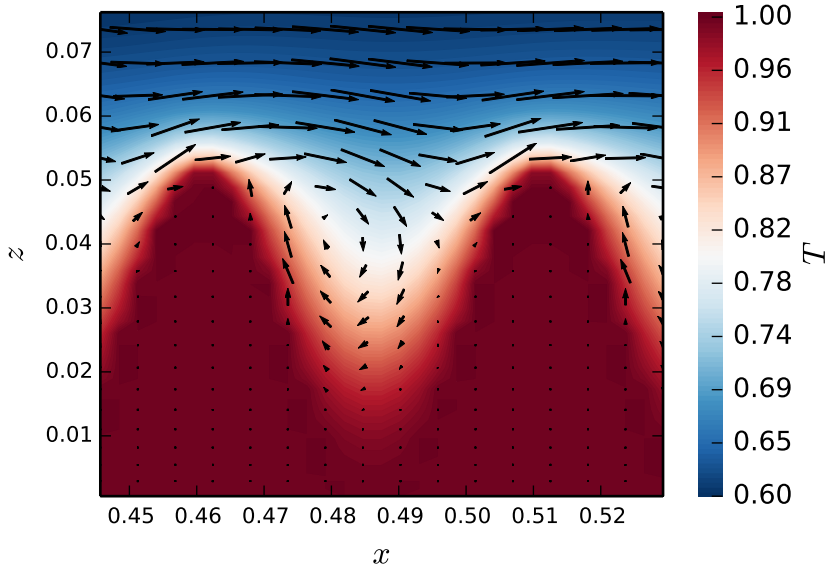

FIGURE 3.7: Detail of the time and space averaged flow field in the cavity of the sinusoidal wave structures. Here we see the main circulation moving perpendicular to the waves, and is almost unaffected by the cavities. In the cavities itself are secondary circulations which resemble typical flow in a cavity circulations.

In Figure 3.5 we have also plotted in blue the Nusselt number compensated with the increase in area by multiplying the Nusselt number with the inverse area increase, A_{flat}/A_{wave}. The compensated heat transfer rate only decreases slightly at low f but after $f = 6$ drops rapidly. There is no optimum visible with the compensated Nusselt number.

For the two dimensional wave pattern, depicted in Figure 3.8, we see a similar trend. First, the value stays more or less the same but after a certain threshold decrease very fast.

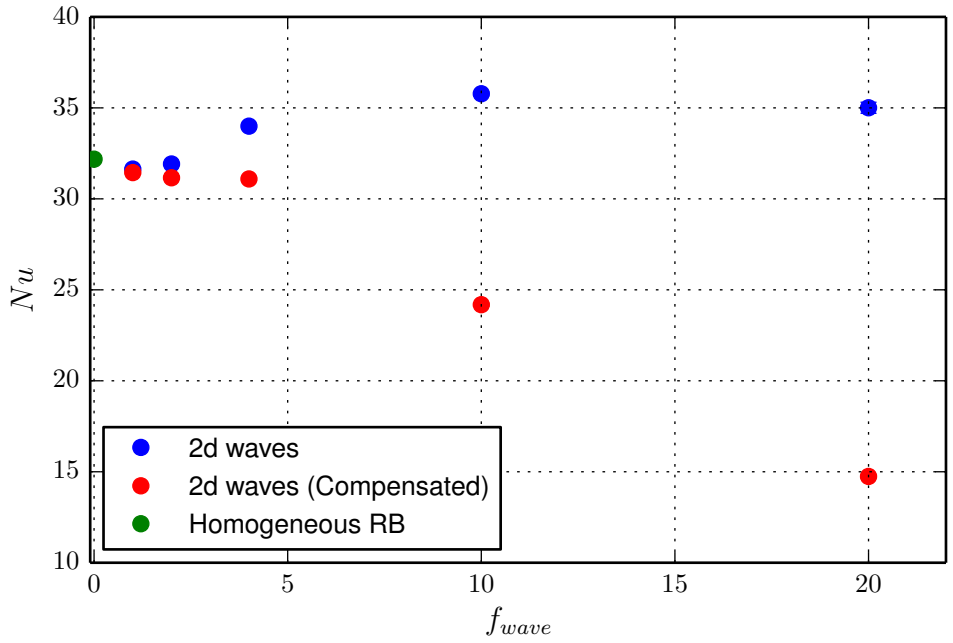

FIGURE 3.8: Nusselt number versus the wave frequency in two dimensions. Blue is the regular Nusselt number, red is the area compensated Nusselt number. For reference, the homogeneous Nusselt number has been plotted at $f = 0$.

When comparing the average bulk temperature for the 1D and 2D wave patterns, there is a slight difference. For low f_{wave} they are more or less equal, but the average temperature of the 2D wave pattern does not reach the same maximum as the with the simulation for the 1D wave pattern.

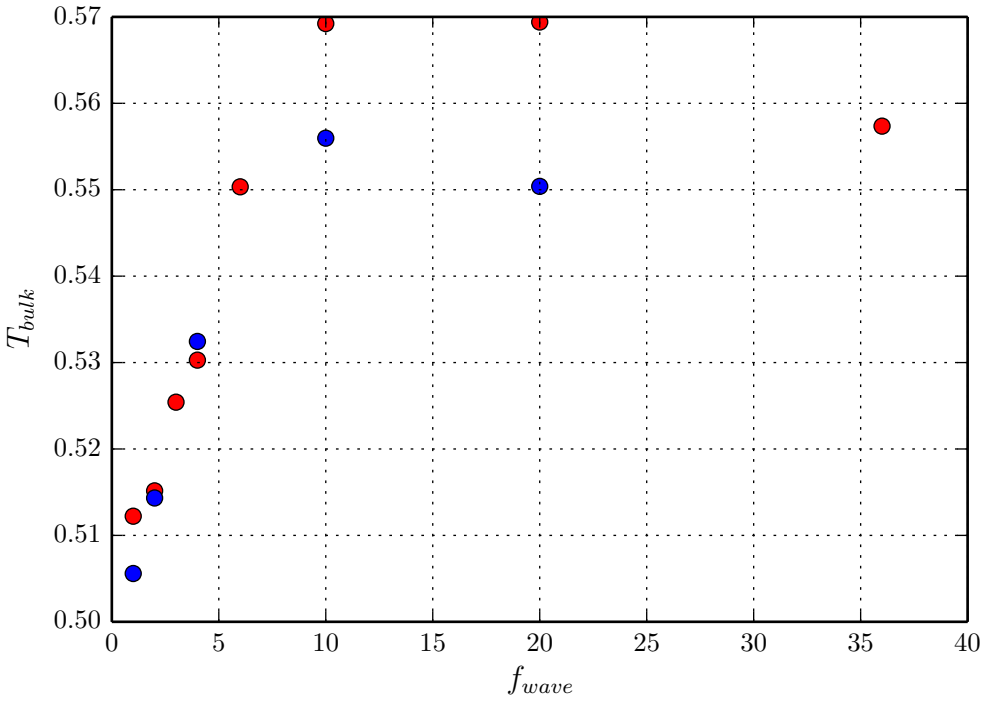

FIGURE 3.9: Average temperature in the bulk versus the wave frequency for the 1D wave pattern in red and the 2D pattern shown in blue. When comparing the 1D pattern with the 2D pattern we can see that it does not reach the same maximum.

3.2.4 Local quantities

Now we will investigate the temperature profiles at the maxima and minima of the pattern structures. The maximum of the structure is the top of the sinusoidal wave. For the 1D pattern this will result in a maxima that will propagate in the complete y-direction. This data will be averaged to find the average temperature profile at the maxima. For the 2D wave, the maximum will be on a single grid point. Now we will investigate the temperature profiles at the maxima and minima of the pattern structures. First we will select the time averaged temperature data exactly at the top and at the bottom of a 1D or 2D wave pattern. If there are multiple maxima or minima, which is the case for $f > 1$ and the 1D wave pattern, those will be averaged to find the average temperature profile at the minimum or maximum of the wave pattern. The result for the 1D wave pattern can be seen in Figure 3.10. Here, the temperature is plotted as a difference with its corresponding wall against the distance from this corresponding wall. As a reference, the temperature difference of the top plate is also plotted in the same figure. For $f = 1$ there is only a small difference in all three temperature profiles. Increasing the wave frequency we see an increase in temperature difference at the end of all profiles. We also see that for almost all cases the temperature profile on the hills of the sinusoidal patterns, shown in red, finally overlap with the temperature profile of the valleys. Another thing to notice is, starting from $f = 6$, the temperature profile of the valleys show first minor inflection points and with increasing frequency, deviating more and more. In the $f = 36$ simulation we see that the profile even stays more or less constant in the beginning.

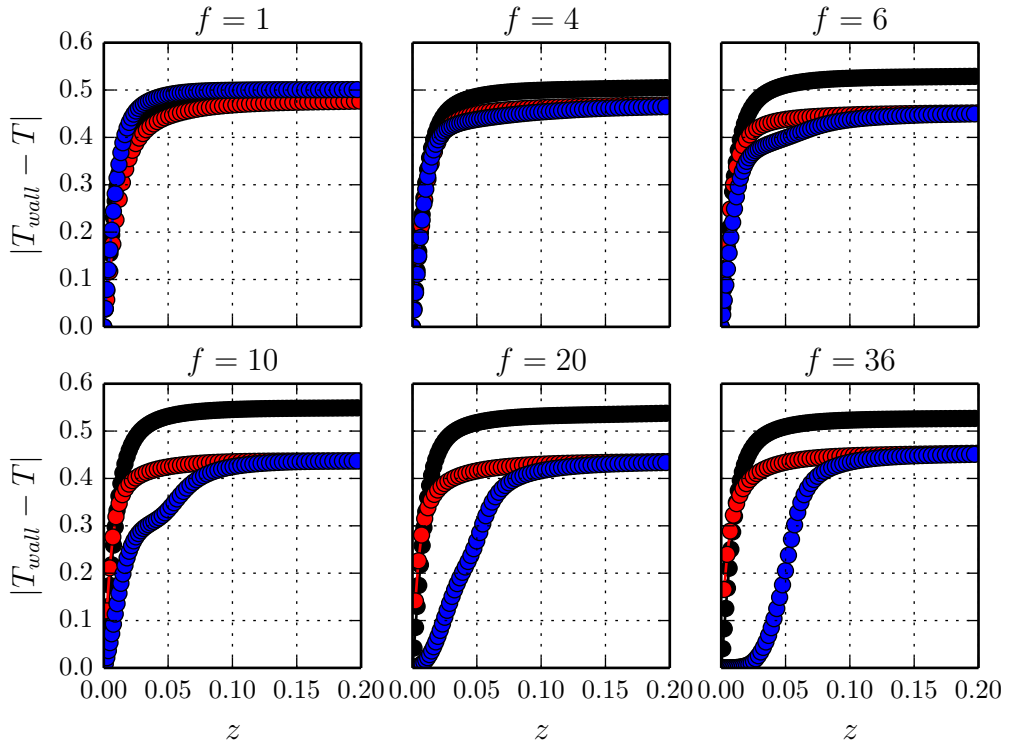

FIGURE 3.10: Temperature difference with the boundary versus the distance to the boundary. The red dots show the average temperature on the hills of the 2D sinusoidal waves, the blue dots show the average temperature in the valley of the 2D sinusoidal waves, and the black dots represents the average temperature difference at the top wall.

The same analysis can be made for the 2D wave pattern. These plots are shown in Figure 3.11. Again the same trend is shown, where at low frequencies all three profiles overlap. Increasing the frequency results again in a small but clear difference at the end of the temperature profiles. When comparing the shape of the valley temperature profiles with the 1D profiles, it seems that for the 2D patterns the same shapes occur with lower frequencies. The shape of the valley profile $f = 10$ of the 2D looks more or less identical to the 1D profile at $f = 20$. Also the 2D valley profile $f = 20$ looks identical in shape to the 1D profile at $f = 36$.

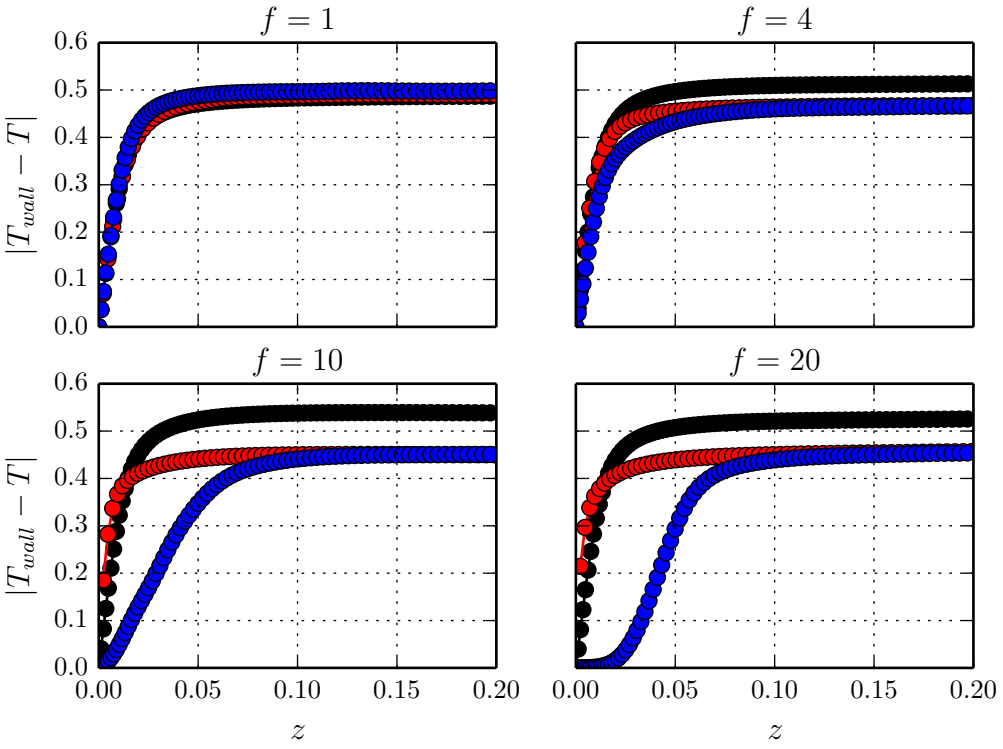

FIGURE 3.11: Temperature difference with the boundary versus the distance to the boundary. The red dots show the average temperature on the hills of the 2D sinusoidal waves, the blue dots show the average temperature in the valley of the 2D sinusoidal waves, and the black dots represents the average temperature difference with the top wall.

3.2.5 Discussion

In this study we added physical roughness to the bottom plate. These roughness elements will have a certain height and therefore, the effective height of the system will be less than the hard coded unity. The height of the system is important for the Rayleigh number, which has the height in its definition. In this definition, the height is cubed, and will have big consequences. The height of the system varies in space and has a maximum of unity in the valley of the 1D or 2D wave patterns and a minimum value of 0.95 on the hills of the 1D or 2D patterns and will change the Rayleigh number locally by the following relation:

$$\mathrm{Ra}_{actual} = (h(x,y))^3 \, \mathrm{Ra}_{input} \tag{3.2}$$

On average, the height of the system is reduced to 0.975. Using the above relation, the actual Rayleigh number when using 10^8 as an input is $9.27 \cdot 10^7$. This is an decrease of almost 7% and we need to keep in mind when comparing this to for example the homogeneous RB case.

The heat transfer of the 1D and 2D stripes are almost the same, with a small advantage to the 1D wave pattern. However, when keeping in mind that the Ra= $9.27 \cdot 10^7$, the Nusselt number is actually too low. For both uncompensated cases, an optimum was visible for the heat transfer. After applying the area increase this optimum was not visible anymore. In Figure 3.6 we could see that the fluid flows downward in the

center of the valley and moving upwards past the borders. This gives the impressing the the fluid makes good use of the additional area and could be a possible explanation for the optimum in the uncompensated data. The uncompensated Nusselt number decreases again after around $f = 10$ for both cases. We saw in Figure 3.7 that there is a secondary circulation between the waved structures. This gives the impression that the heat transfer is not as efficient as the heat has to pass through this secondary circulation. Another reason can be that the cavity that is created, is getting smaller as we increase the frequency. The smaller cavity makes it more difficult for the fluid to flow as the no slip boundary is closing from multiple sides. This might be a reason for the uncompensated Nusselt number to decrease. The compensated Nusselt numbers for both, the 1D and 2D wave pattern are almost identical.

The average bulk temperature of the fluid is for lower frequencies almost identical for the 1D and 2D wave pattern. From these simulation we saw that for $f = 10$ and $f = 20$ is slightly lower. Both curves showed a small optimum around $f = 10$. A possible explanation could be that these frequencies have the optimal dimensions for the flow to use the additional surface, which we also saw in Figure 3.6. The higher frequencies had a less optimal flow observed which could be the reason for less heat entering the system and therefore a lower average bulk temperature.

The temperature at the top and bottom of the sinusoidal wave pattern are almost identical for lower frequencies. At lower frequencies, the flow is less obstructed and when zoomed in very locally, there is not much difference with both positions. When increasing the frequency, the wall come closer to the valley, and this increases the difference between the to positions. Eventually, when the frequency is high enough, the valleys approach a cavity flow situation. This might possibly be a reason why at the highest frequencies the flow stays substantially hotter, as can be see in $f = 36$ of Figure 3.10.

Another thing we see from the same graph is that the temperatures deviate from each other when comparing the top plate with the bottom plate. A possible explanation for this could be that we are breaking the symmetry of the system by including the wave pattern on the bottom plate. At $f = 1$, both, the top and bottom plate profiles end in more or less the same line. It is well known that for the homogeneous RB case, the temperature of both profiles should be 0.5. In this case, $f = 1$ is quite close to the homogeneous case and the profiles are not that different. As we have increased the frequencies, we make the system more and more asymmetric. This might explain the increase in difference of the profiles of the top and bottom plate. On the last graph, at $f = 36$, we see that the profiles move closer again. Possibly because the cavities are reduced to such a size that they cannot be used efficiently anymore. This reduction in heat transfer, might be the cause for the profiles to move closer together again.

3.3 Other structures

Several other structures have been coded, such as triangle waves, single spots, arrays of spots, and tetrahedrons. Most of these structures were used in preliminary tests to investigate the global effect on the large scale circulation. Only the triangle wave pattern has had a full comparison with the sinusoidal wave pattern.

3.3.1 Triangle wave pattern

One of the other patterns that have been analyzed is the 1D triangle wave pattern. As with the 1D sinusoidal wave, it propagates in a single direction. To parameters for the simulations, such as amplitude, Rayleigh number, and Prandtl number are kept the same as the 1D sinusoidal wave to compare both cases. The typical geometry is depicted in Figure 3.12.

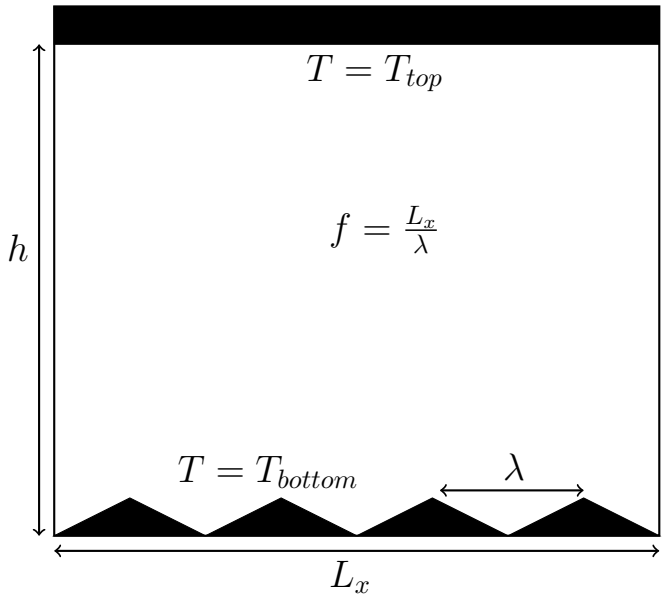

FIGURE 3.12: The 2D projection of geometry used for the physical roughness triangle wave pattern simulations. The structures are only present on the bottom plate which has the temperature set to T_{bottom}. The top plate is flat and has the temperature set to T_{top}. The triangle wave pattern only varies in the x direction and is equal for all y.

For additional insight, plots of the instantaneous temperature field have been created. These are shown in Figure 3.13.

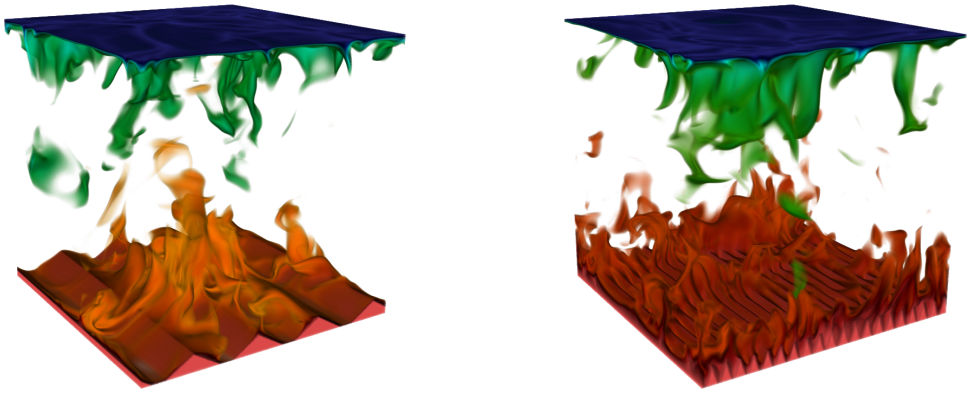

FIGURE 3.13: Snapshot of the instantaneous temperature field for $f = 4$ and $f = 20$ triangle wave patterns.

In Figure 3.14 we compare the Nusselt numbers of the triangle wave system with the sinusoidal wave system. For the lower wave frequencies we do not see a lot of difference between both systems. Only for $f = 6$ and $f = 10$ we have a slight difference with the advantage for the sinusoidal wave.

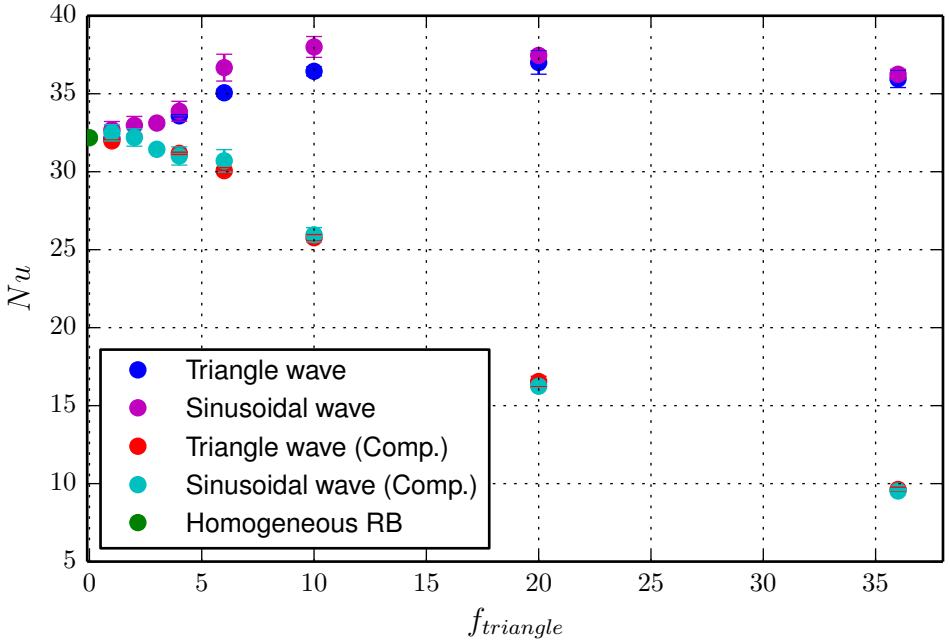

FIGURE 3.14: Comparison of the Nusselt numbers of the triangle and the sinusoidal wave, for both the compensated and uncompensated data.

This outcome is not as was expected as it was thought that the triangle structures would have an advantage. These structures have a peak, which could act as a nucleation point for the ejection of plumes. When looking at the peaks we see indeed that the flow prefers to move upward at the peak of the triangle wave, however the same is also observed at the sinusoidal wave.

The temperature profiles, which are shown in Figure 3.15, look also identical to the sinusoidal waves. In the lower frequency part we see an overlap of all the temperature profiles. Increasing the frequency, again, increase the difference in temperature of the top and bottom plate. We also see a stagnation of temperature between the gap of two triangles in $f = 36$.

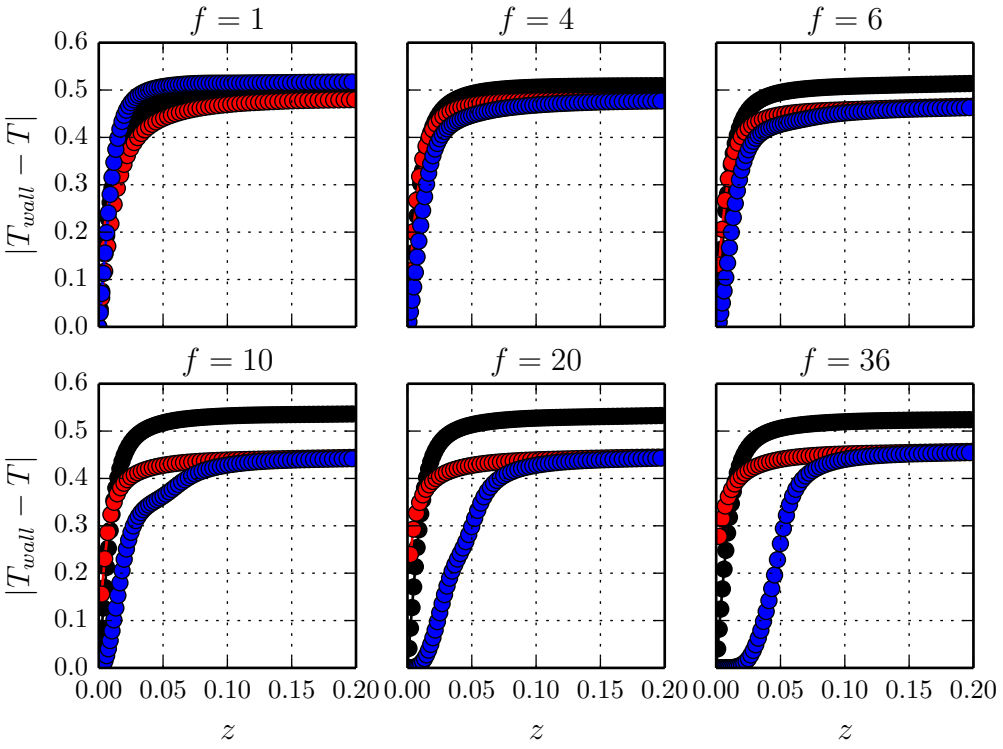

FIGURE 3.15: Temperature difference with the boundary versus the distance to the boundary. The red dots show the average temperature on the hills of the 2D sinusoidal waves, the blue dots show the average temperature in the valley of the 2D sinusoidal waves, and the black dots represents the average temperature difference with the top wall.

These tests with the triangle pattern are still preliminary and more work needs to be done. As we are increasing the frequency, the angle of the triangle also changes. It would be interesting to see if there is an optimal angle for nucleation. We saw that there is not a big difference between the triangle and sinusoidal wave. A possible reason could be that for a very rough approximation we could use a triangle wave as a substitute for the sinusoidal wave. In the valleys, the triangle wave will be a bit too high, and on the hills it will be slightly too low. This will result in a slight difference in the local Rayleigh number. This could partly explain the minor difference.

3.3.2 Single roughness elements

We started this study by using single roughness elements. These were used as an possible analog to the inhomogeneous temperature boundary conditions where artificial roughness was simulated by heating a single spot on the boundary layer. These spots were varied in width and height to see what the effect was on the large scale circulation.

After various test we did not see anything special. The large scale circulation placed itself in a favorable manner but we saw no dependence in position by this single roughness element. In some simulations it seemed that the circulations position itself in a certain way. However, moving the element to another position showed that this was not reproducible and most probably a coincidence.

The same elements were also placed in small arrays, consisting of five or nine roughness elements. By placing them in a cross-like fashion we hoped to affect the large scale circulation. However, again this did not seem to work. The large scale circulation placed itself randomly, and is not affect by the array of roughness elements.

By introducing more roughness elements we saw a slight increase in Nusselt number, but we have to keep in mind that we have increased the area of the bottom plate. This is probably one of the reasons for the small increase.

3.4 Conclusions

As an analog to the first chapter, we have studied the possibility to position of influence the LSC with a single roughness element. These elements were varied in height to a maximum of 0.05, which is more than twice the thermal boundary layer thickness. As in the previous chapter, we did not find a reproducible configuration for the HS to observe any significant influence. Also placing small arrays of roughness structures did not influence the flow dynamics. We did observe a slight increase in Nu, but this could be related to the increase in heated area. The exact details are still open to be investigated.

The main focus of this chapter is to study the effect of 1D and 2D waved patterns on global and local flow quantities of the system. These waved structures had an amplitude of 0.025, with its valley set to the bottom of the system. This sets the peaks of the waved pattern at a height of 0.05. The frequency of the pattern is varied in such a manner that only complete wave lengths fit in the system. For the 2D system, the same frequency is used for both directions.

When comparing the Nu for the 1D and 2D systems, we observed no significant difference. Both systems showed an increase in heat transfer, by increasing f, until an optimum is reached. After this optimum, the heat transfer decreases again. It is suspected that the flow can take advantage of the additional area for lower f, while for higher f, the cavities between the waves restrict the flow to effectively use the additional space. When compensating the Nu for the additional area, the optimum disappears and both, the 1D and 2D patterns decrease rapidly after $f = 6$. The simulations all used $Ra = 10^8$ and $Pr = 1$, however, the roughness elements reduce the height of the cell locally and therefore, effectively reduce the Ra by 7%.

The temperature difference from both walls were almost equal at $f = 1$. Increasing f, we saw an increase in difference from both profiles. At $f = 36$, this difference seemed to reduce again. This is however not perfectly clear. To confirm this trend, additional simulations with higher f are needed.

As a preliminary investigation, triangle waves have been simulated. It has been reported that these sharp geometries are beneficial for plume generation and therefore, increase the heat transfer of the system [13]. From these simulations, we see no significant difference between the triangle and the sinusoidal wave. The Ra used in our simulations are however much lower than the ones used in the reference. The flow dynamics at the vicinity of both structures are still in need for study and more work needs to be done.

CHAPTER 4

Mixed insulating and conducting boundary conditions

4.1 Introduction

4.1.1 General Introduction

In a third study we look at the effect of mixed insulating and conducting boundary conditions. This study has been performed in parallel to the other two chapters and has no direct relation. The mixed conditions will only be applied to the top plate and will add a certain degree of inhomogeneity to the system.

The importance of this problem can be motivated by various geophysical applications. For example, ice floes in the arctic regions, which are floating slices of ice, act as almost perfect insulators to the heat flux. It was recently shown [16], that the size distribution of leads, which are fractures in ice floes, is multi-scale, and that the size has clear influence on the heat flux. The showed that smaller leads, the size of a few meters, are more efficient in heat transfer than bigger leads, the size of a few hundredths of meters.

The problem has already been studied in [17] in two dimensions. Their focus was primarily to quantify the effect of the surface heterogeneities on the critical Rayleigh number. They also explored the high Rayleigh number regime, which matches the Rayleigh number of our study. In this chapter we will extent this study to three dimensions and focus on the effect of the composition of these patterns on the Nusselt number, at $Ra = 10^8$.

4.1.2 Program modifications

To simulate the different mixed insulating and conducting patterns we have again modified the 3D Rayleigh-Bénard Cartesian finite difference program. As a basis the semi-staggered program has been used. This code parallelizes the domain in slabs which are stacked in the z direction. The reason for choosing this code is that the quantities are fully staggered and are placed in a beneficial way in the simulation cell which makes it easier to set Neumann boundary conditions. Figure 4.1 shows a 2D projection of the simulation cell with the location of all the quantities.

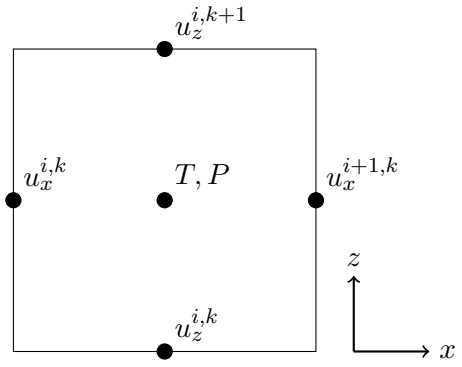

FIGURE 4.1: Location of all the quantities in the simulation cell projected in 2D. The velocity vectors are placed on the border of the cell and the temperature and pressure are place in the cell center.

To make it possible to create different insulating and conduction patterns we need an additional two dimensional input array at each boundary which indicates if that grid points are adiabatic or conducting. If a point is adiabatic, no heat flux is exchanged with the boundary. This is used when calculating the second derivative. Equation 4.1 shows the general equation, with the prefactors left out. If the boundary is set to adiabatic, $\frac{\partial T}{\partial z}|_+$ is set to zero. An overview of the grid points near the boundary is shown in Figure 4.2.

$$\frac{\partial^2 T}{\partial z^2} = \frac{\frac{\partial T}{\partial z}|_+ - \frac{\partial T}{\partial z}|_-}{\Delta z} \tag{4.1}$$

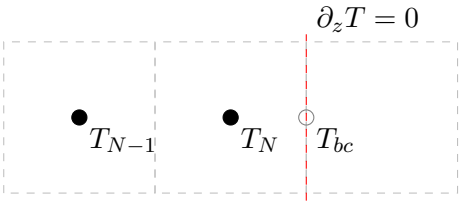

FIGURE 4.2: An overview of the last grid points and their relative distances.

Again the part which computes the statistics of the program has been extended to include time averaged 3D statistics. All velocity vectors and the temperature are written to a HDF5 file for possible post processing. The time averaged quantities Tu_z and T^2 are also stored for possible processing.

4.2 Insulating stripes

4.2.1 Geometry and simulation domain

For this simulation different patterns have been investigated. First a pattern has been introduced that only has a variation in a single dimension in a stripe-like fashion. The typical geometry of this setup used is depicted in Figure 4.3. The inhomogeneities are restricted to only the top plate ($z = h$) and are created by alternating adiabatic

regions ($\partial_z T = 0$) with conduction regions ($T = T_{top}$). The bottom plate is kept at constant temperature ($T = T_{bottom}$). The code is again based on the classical Oberbeck-Boussinesq approximations seen in Equation 1.4. The boundary conditions are periodic in both horizontal directions. The stripes have a wavelength L_p and is directed in the x-direction. The wavelength of the stripes is set in such a manner that the conduction area is always exactly the same size as the adiabatic area. The periodicity can be described in the following manner:

$$\begin{cases} T(x,y,h) = T_{top} & \forall x,y \in [jL_p, L_{p2} + jL_p], j \in \mathbb{Z} \\ \partial_z T(x,y,z) \mid_{z=h} = 0 & \forall x,y \notin [jL_p, L_{p2} + jL_p], j \in \mathbb{Z} \\ T(x,y,0) = T_{bottom} & \forall x,y \end{cases} \tag{4.2}$$

The number of stripes will be a discrete parameter for the system which will set the wavelength. We restrict ourselves in keeping the area of the insulating an conducting stripes equal. The number of stripes is defined in such a way that one stripe includes one conducting stripe and one insulating stripe. This can also be seen as the frequency (f) of the system. As it is a discrete value we will automatically fulfill that the area is equal. However, as we have a limited amount of grid points this will limit the choice in the number of stripes. For convenience we convert these discrete values into the continuous wave number k_s which is defined as $2\pi N_{stripes}/L_y$.

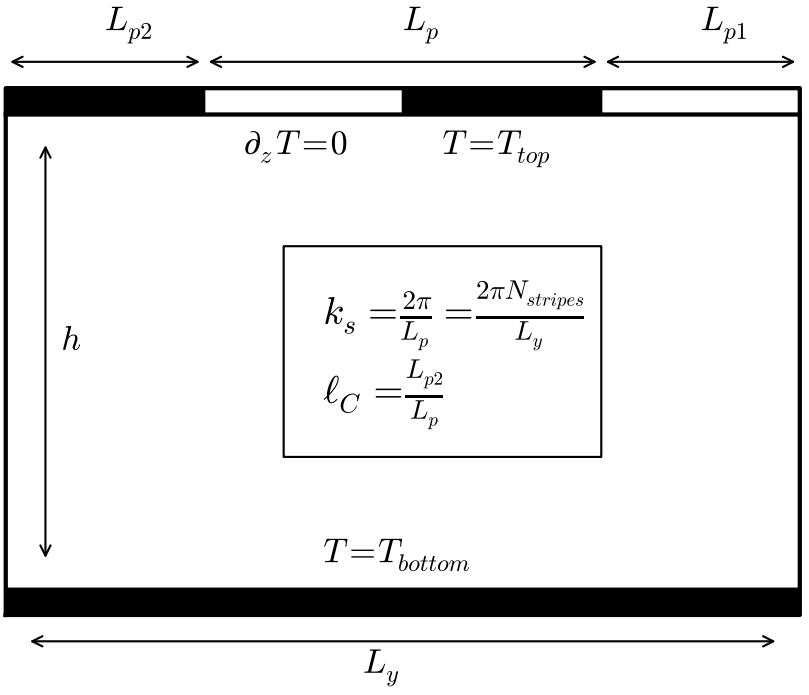

FIGURE 4.3: The 2D projection of geometry used for the stripes simulations.

The height domain for all simulations has been set to unity. The grid has again been set to $361 \times 361 \times 289$ which has proven to be a fine enough grid for our low Rayleigh simulations. Both aspect ratios are also set to unity giving a cubic box. As the aspect ratio are rather small there could be an issue with the aspect ratio dependence on these lower Rayleigh number simulations. Therefore, as a test case, a simulation was run on aspect ratio 1 and using the same conditions a simulation was run at aspect ratio 2. The

difference in Nusselt number between the two tests was $< 1\%$ which indicates that for this Rayleigh number the grid can be considered independent of the aspect ratio. The same test has been done with a Rayleigh number set to 10^6 and here it was clearly not the case. Therefore, the simulations with the Rayleigh number set to 10^6 have not been used. All test details are shown in Table 4.1.

Ra	Γ	$N_x \times N_y \times N_z$	Nu
10^6	1	$121 \times 121 \times 145$	9.39 ($\pm$0.13)
10^6	2	$241 \times 241 \times 145$	8.94 ($\pm$0.27)
10^6	3	$361 \times 361 \times 145$	8.40 ($\pm$0.11)
10^8	1	$361 \times 361 \times 289$	26.10 ($\pm$0.02)
10^8	2	$721 \times 721 \times 289$	26.89 ($\pm$0.23)

TABLE 4.1: Aspect ratio test details. All simulations used twenty sets of stripes at which the size was kept equal. Prandtl was set to 1. For the Rayleigh 10^6 we cannot conclude which aspect ratio is enough. For Rayleigh 10^8 we do not have a decreasing trend and the aspect ratio of 1 seems acceptable.

4.2.2 Flow visualization

One of the difficulties is to visualize the flow field. Figures, shown on paper on screens are always two dimensional and the data created here is in three dimensions. Still to give a feel for the flow field, snapshots have been created from the temperature field. These are created from the instantaneous fields of the $f = 4$ and $f = 20$ stripes simulations and are shown in Figure 4.4.

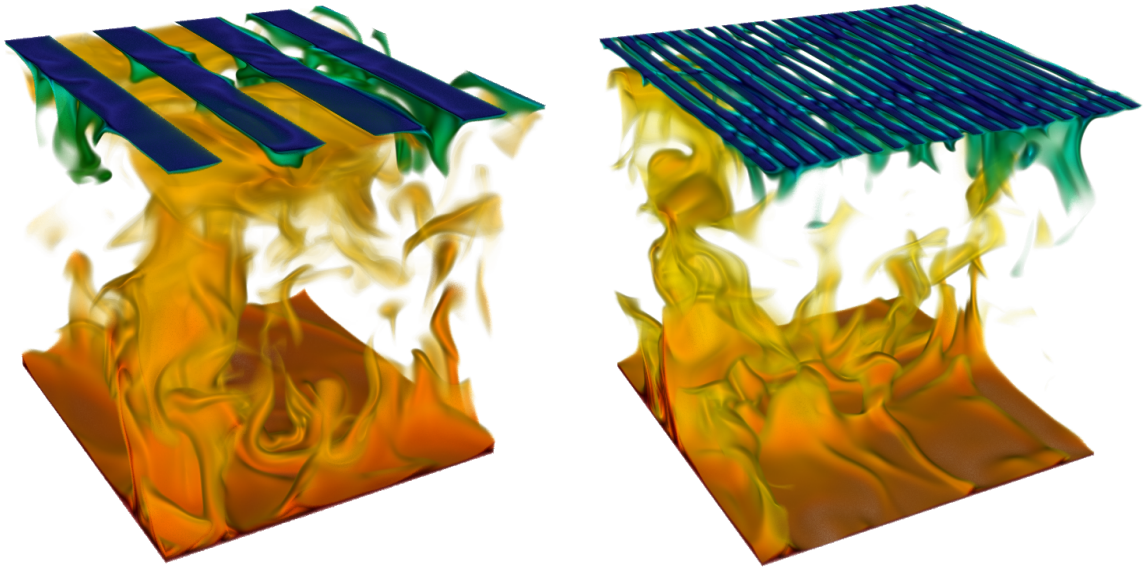

FIGURE 4.4: Snapshots of the instantaneous temperature field for $f = 4$ and $f = 20$ conducting/insulating stripes.

4.2.3 Global quantities

One of the first questions we want to address is the influence of these stripes on the heat transfer. Heat is injected from the bottom plate and is transported by the fluid to the top

plate where it can exit the system. Now we restrict the system from removing the heat by making half of the top plate adiabatic. This will of course have an effect on the heat transfer. The heat transfer is plotted against the wave number in Figure 4.5. The error bars have been calculated from the statistical convergence error. Not all simulations have an optimal convergence but the results have been deemed acceptable for these plots. As we have multiple decades of the data, it is presented in a semi-logarithmic plot.

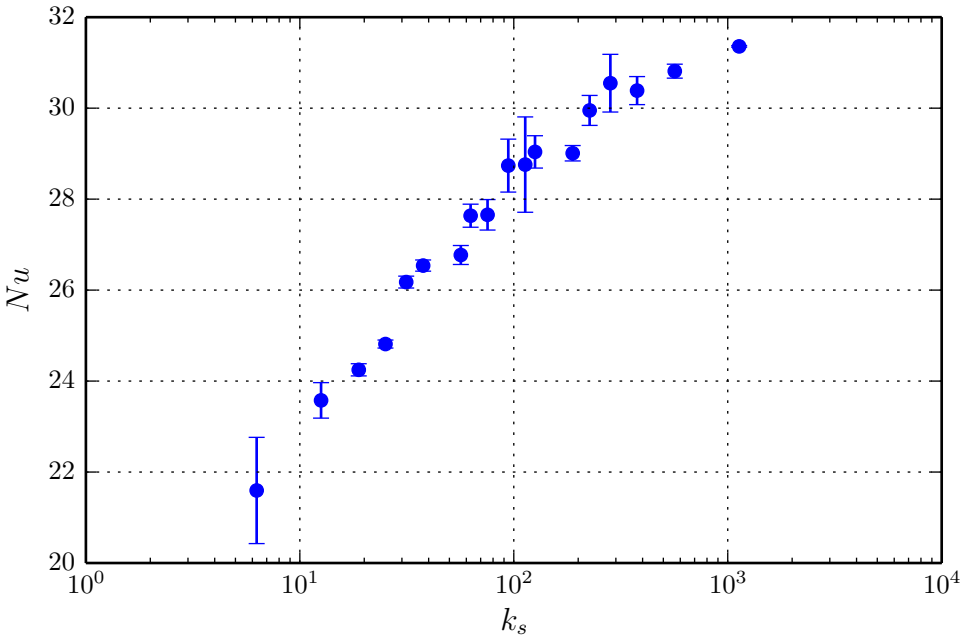

FIGURE 4.5: Wave number versus Nusselt number. Error bars are based on the statistical convergence of the data.

When looking at the data we see that when having only a single stripe frequency ($f = 1$), meaning we have divided the top late in two equal areas, the Nusselt number is just below 22. This is around two thirds of the Nusselt number of the homogeneous case which is $32.1(\pm 0.06)$. Now when we increase the wave number, and therefore, increase the number of stripes, the Nusselt number goes up. The last point of the graph at a wave number of approximately 1131 a set of stripes is using exactly two grid points, one for each type. At this point the Nusselt number is 31.3 which is almost the homogeneous case.

For the bulk temperature, which is plotted in Figure 4.6, we see the same kind of trend. At the first data point we see that the temperature is around two thirds of the temperature of the bottom plate. However when we increase the the wave number the bulk temperature goes down. At the last data point, were we again have the maximum number of stripes possible, the bulk temperature is very close to the homogeneous case where we expect a temperature of 0.5.

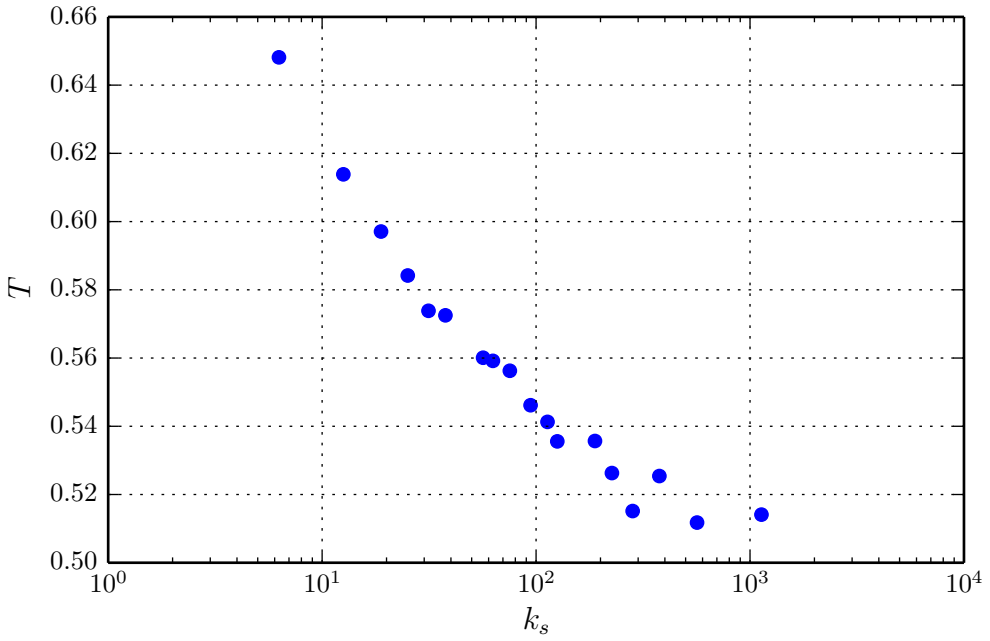

FIGURE 4.6: Wave number versus the bulk temperature.

Only the $f = 1$ simulation had a clear effect on the large scale circulation. The average downward flow has positioned itself in the center of the conducting area and the average upward flow was on the adiabatic region. Again the two average ejecting regions are positioned in such a way that the distance is maximized. Figure 4.7 shows how the $f = 1$ is dividing the top plate equally in half and how the large scale circulation positions itself in the system.

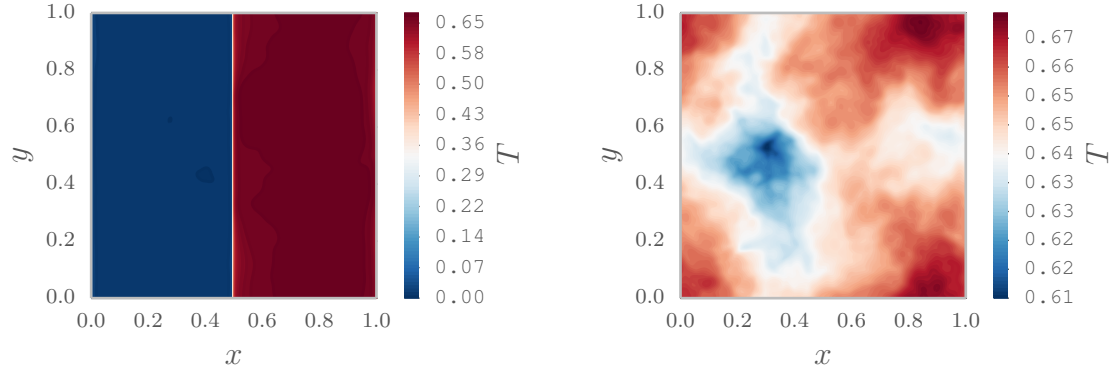

FIGURE 4.7: Left: a time averaged temperature slab, exactly at the border, indicating the blue conducting area and the red insulating area. Right a time averaged temperature slab exactly in the middle of the system. Not very surprising, there is an averaged flow downwards below the conducting stripe (blue spot) and an average flow moving upward on the top and bottom right corners (red spots).

4.2.4 Local quantities

Now we focus on the local quantities. One of the interesting quantities is the temperature close to the adiabatic wall. As there is no direct heat transfer possible at this position we expect the temperature to be much higher than at the conducting wall. The only heat transfer that is possible is through convection of the fluid. The temperature is not constant at the adiabatic region. Close to the border of the adiabatic region it will change in a continuous manner to the conductive counterpart. To give an insight on the temperature at the adiabatic and conduction region we have calculated the average of all adiabatic- and conducting stripes and plotted these against the wavelength in Figure 4.8 and Figure 4.9. By using the wavelength it is possible to compare the stripes from the different frequencies with each other. The data from $f = 90$ and $f = 180$ have not been included in the plot as these are a straight line and a single point only.

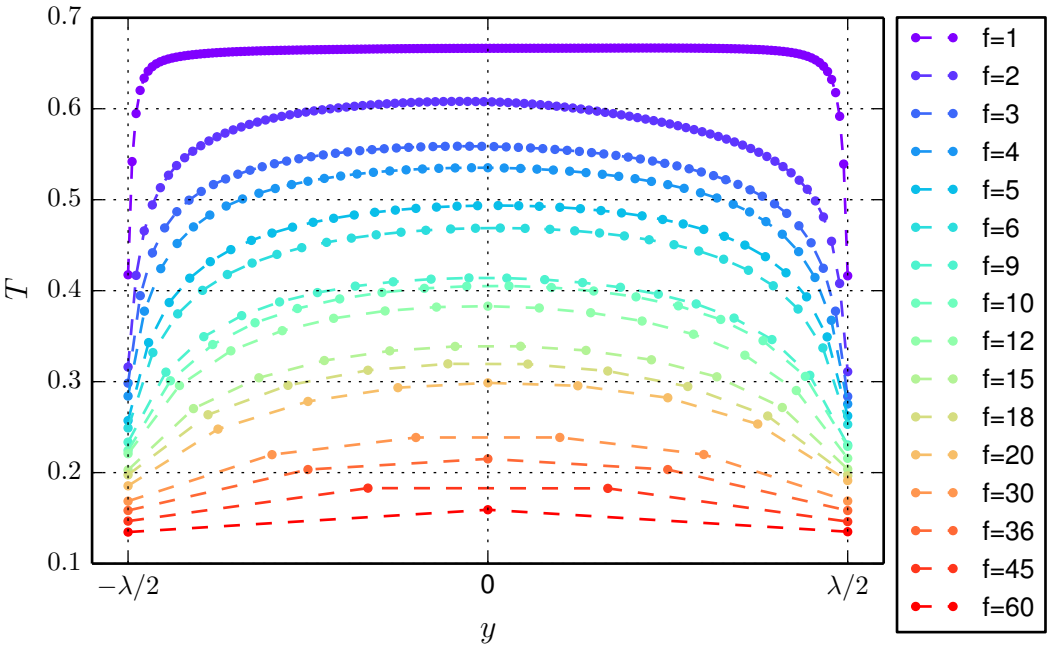

FIGURE 4.8: Temperature at the insulating wall, averaged over all stripes, in time and in the x direction for various frequencies.

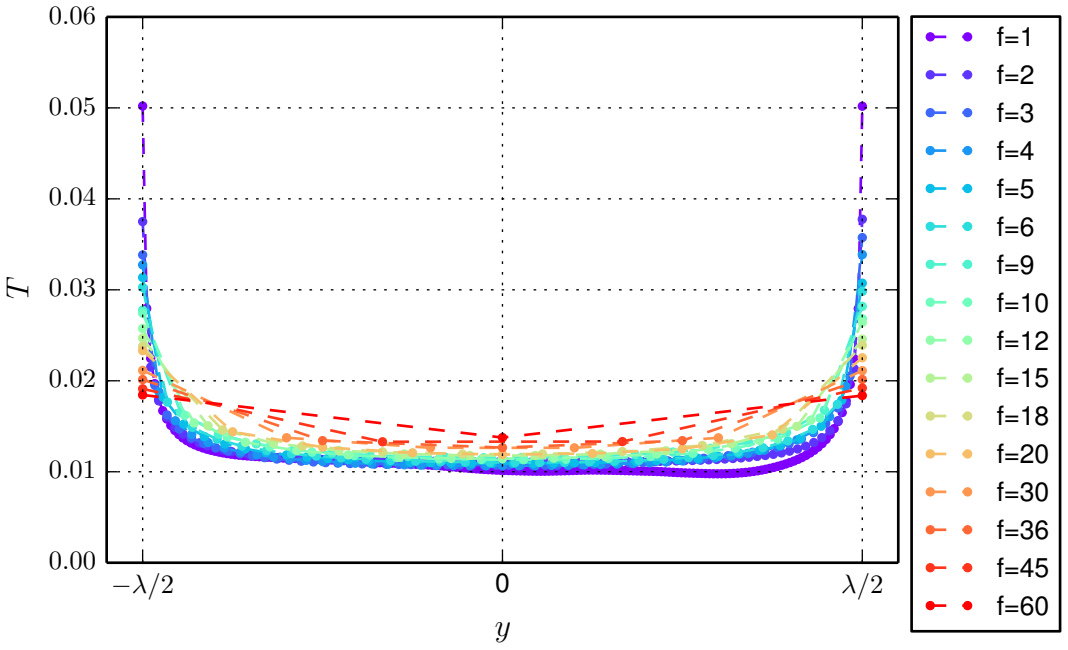

FIGURE 4.9: Temperature at the conducting wall, averaged over all stripes, in time and in the x direction for various frequencies

As we would expect and Figure 4.8 shows, the temperature drops as we increase the number of stripes. A simple explanation could be that the effective area of each individual stripe is reduced when we increase the number of stripes. The total area is divided by a higher number of stripes, resulting in a net lower area for each stripe. The lower frequencies have a maximum averaged temperature that is close the bulk temperature. However, this diverges rapidly when increase the number of stripes. For $f = 1$ it is even slightly hotter than the average bulk temperature.

For the conducting stripes we see a similar but reversed trend. The temperatures are almost zero. They are not exactly zero because the grid point is not exactly defined at the border but in the center of the simulation cell. When the number of stripes is increased, the average temperature also rises slightly. A reason for this could be the influence of the adiabatic stripes which are getting closer with increasing number of stripes. Another reason is that when we increase the number of stripes, the Nusselt number goes up. The Nusselt number is defined as $Nu = T_N/dz$, dz is the fixed cell height, and T_N is the temperature in the last cell, so when the Nusselt number rises, the temperature also has to rise.

Averaging the temperature of the insulating stripes to a single value gives us the possibility to plot this against the wave number of the stripes. Again, as we have multiple decades of data we have presented it in a semi-logarithmic plot shown in Figure 4.10.

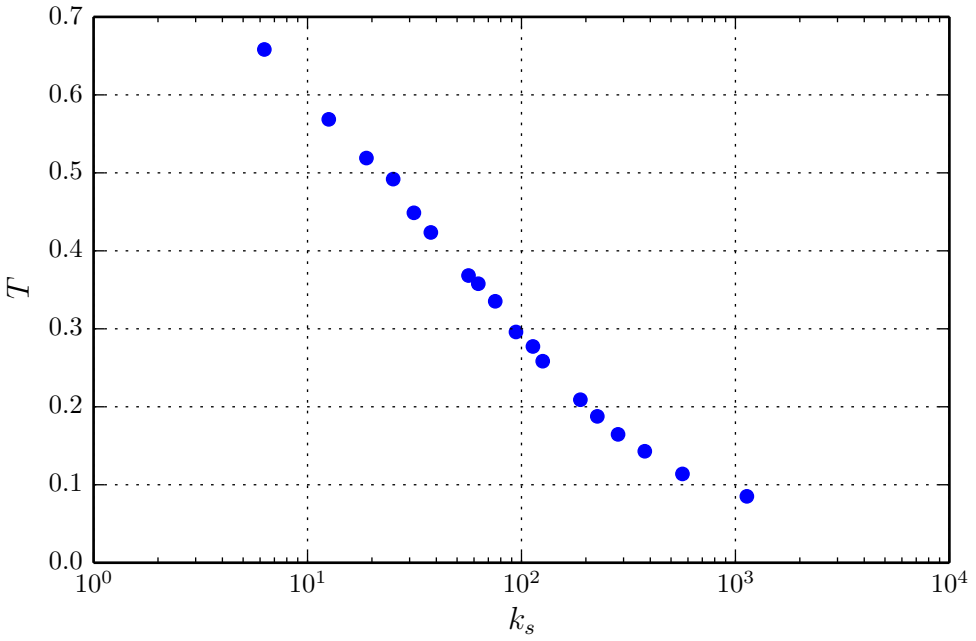

FIGURE 4.10: Stripes vs Temperature

Next, we are use a Fast Fourier transform to convert the data to the frequency domain. This will result in Fourier spectra in which we should see the periodicities that we have placed onto the top plate. It will be interesting to see how these structures hold when moving away from the wall.

In the former plots we used time averaged data to see the various effects. However, performing a Fourier transform on time averaged data is a bad idea as the time averaging before a Fourier transform suppresses the higher frequencies resulting in a biased plot. Therefore, the Fourier transform should be done before the averaging is done. The Fourier transformation has been performed on the instantaneous data. These spectra have been averaged in time and over the y-axis. The results for various stripes near the wall can be seen in Figure 4.11.

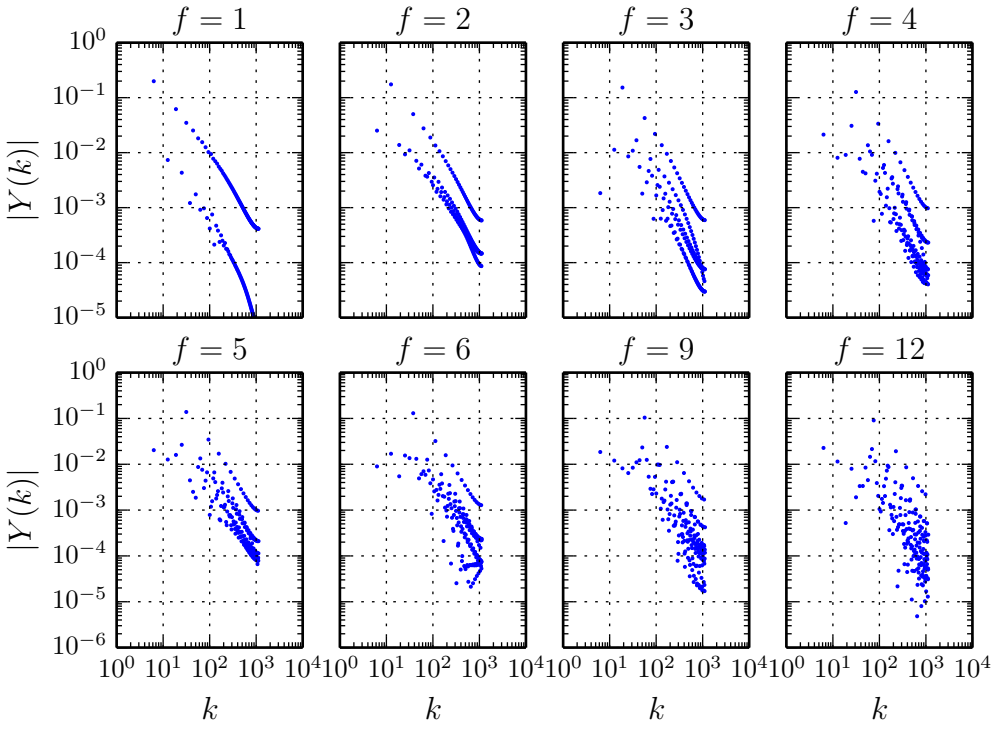

FIGURE 4.11: Two dimensional fast Fourier transform for various stripes, close to the top boundary, averaged in time and in the y direction.

When looking at the simulation with a single set of stripes ($f = 1$), we can clearly identify two dominant lines. When the number of stripes is increased more lines are added to the graph. As some lines overlap it is hard to identify single lines but every increase in stripes, adds two lines to the plot. Eventually there is so much overlap that there are no individual lines visible.

It would be interesting to see how these structures behave when we gradually move away from the border. For this we use the $f = 1$ simulation and perform the fast Fourier transform on various distances away from the border. The results are shown in Figure 4.12.

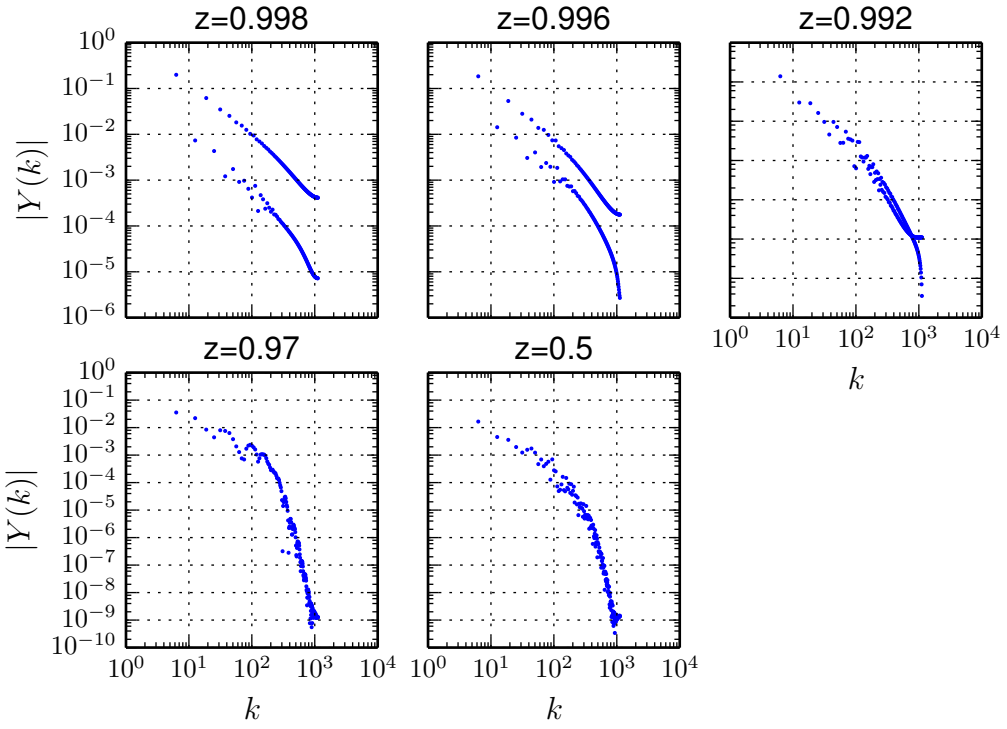

FIGURE 4.12: Two dimensional fast Fourier transform from the $f = 1$ simulation at different z coordinates, averaged in the y direction.

Here we clearly see that the impact from the stripes decrease when we move further away from the border. From z=0.998 to z=0.996, which is only a single grid point farther from the border, the lines decrease almost half in distance apart. At z=0.992 they almost overlap completely and at the last two plots it is hard to imagine that there have been two lines at all. This same trend can be seen with the $f = 4$ simulation which is plotten in Figure 4.13.

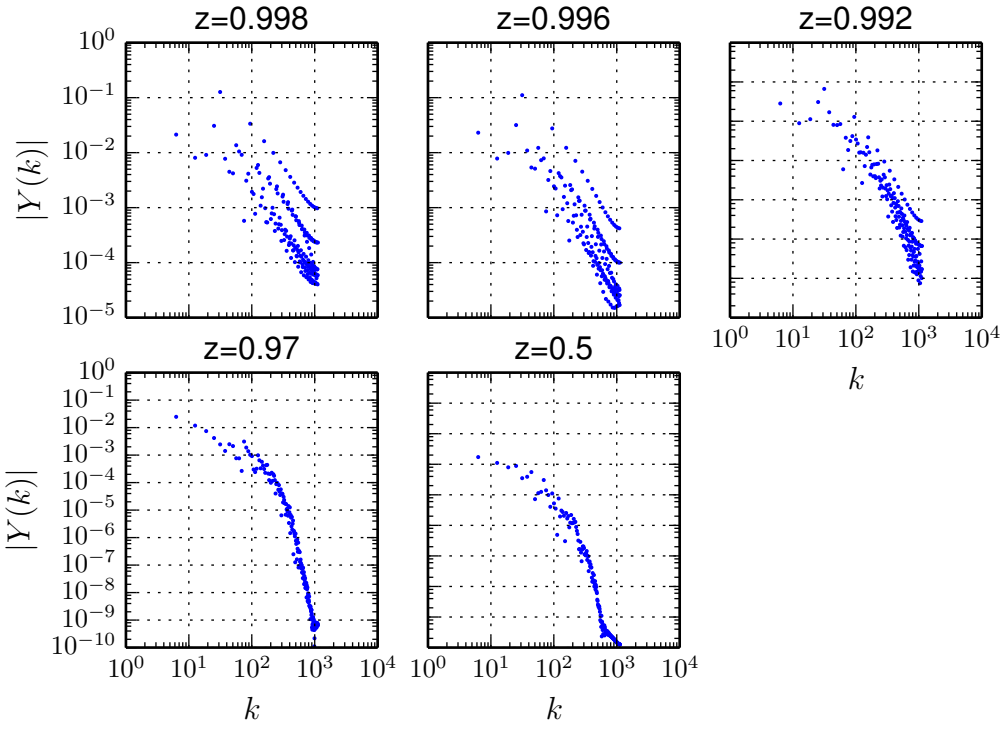

FIGURE 4.13: Two dimensional fast Fourier transform from the $f = 4$ simulation at different z coordinates, averaged in the y direction.

We can also look at the difference between the vertical temperature profiles close to the border for the adiabatic region and the conducting region. As a comparison, the profile from the bottom plate has been added to the plot. The results for various stripe frequencies are plotted in Figure 4.14.

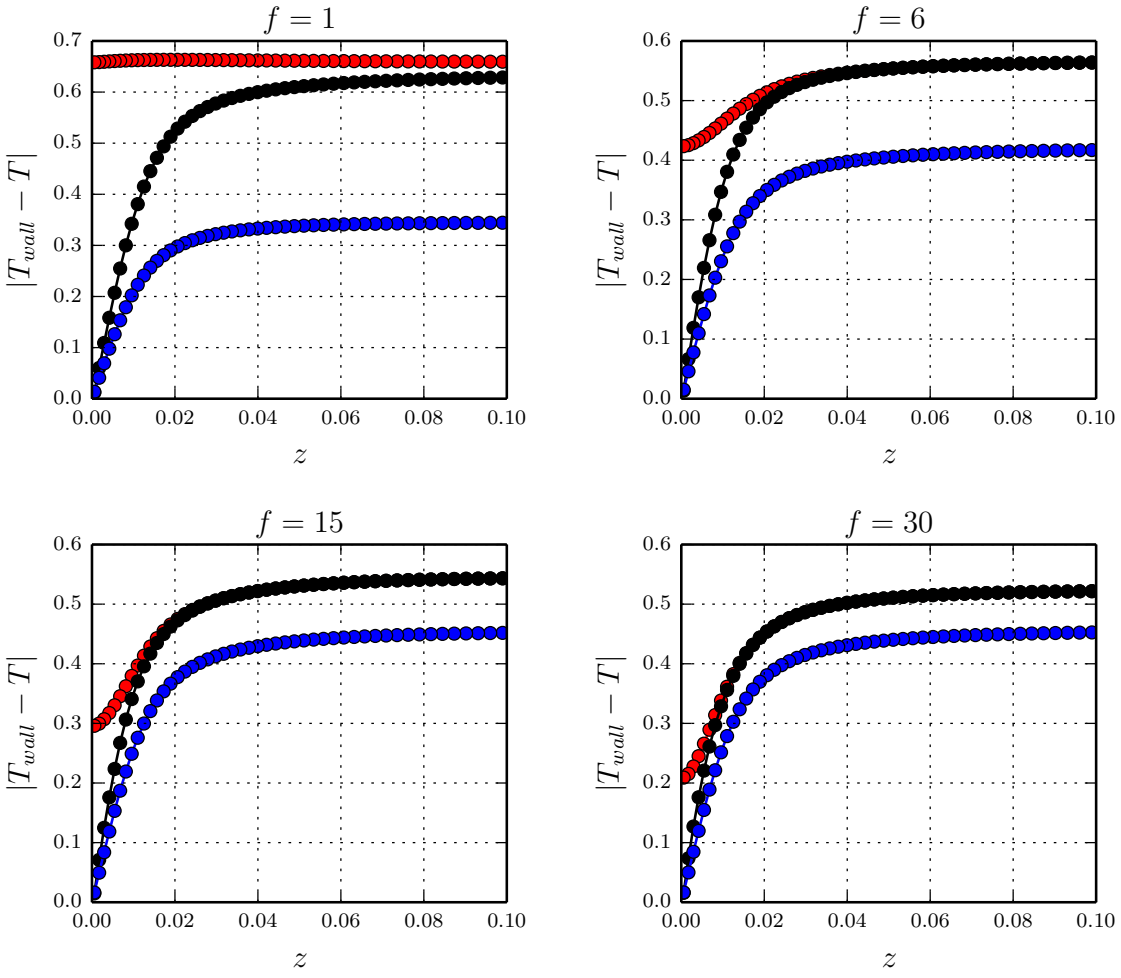

FIGURE 4.14: The average temperature difference from the wall of various checkerboard frequencies. The adiabatic plate area (red dots) and the conducting area (black dots) are plotted as differences from the wall. The bottom plate temperature profile (blue dots) are reversed in temperature, $T(z) = 1 - T(z)$.

4.2.5 Discussion

When looking at the heat transfer of the extreme case for a single stripe we found the Nusselt number to be approximately two third of the homogeneous RB case. The same goes for the bulk temperature which also is around two thirds of the homogeneous RB case. We know from classical RB that due to symmetry of system the bulk temperature is exactly between T_{top} and T_{bottom}. Now that we are introducing stripes we break the symmetry and this easy argument cannot be used. The bulk temperature cannot simply be expressed in a function that is only dependent on plate temperatures and the stripe frequency. Also parameters such as the Rayleigh and Prandtl numbers are relevant. Figure 4.15 shows a simple diagram which compares the classical RB with the single stripe system.

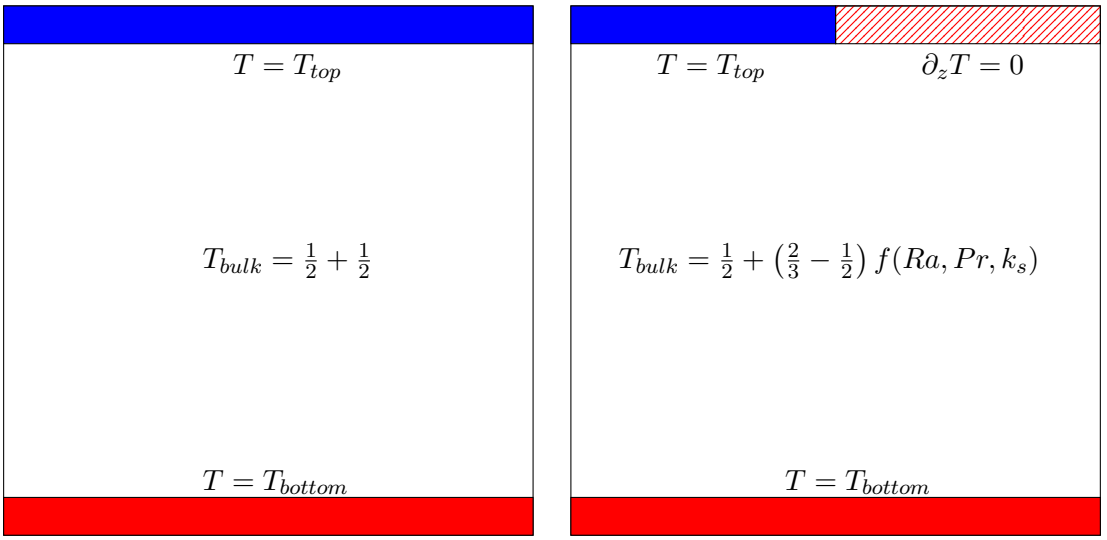

FIGURE 4.15: Left: simple diagram showing a classical RB system with the symmetry argument. Right: The same type of diagram for the system with a single stripe.

The function f is still an unknown function. For these simulations we did not vary Rayleigh nor Prandtl and therefore we cannot exactly predict its behavior. However, we can have a look at the extreme cases. When the wave number k_s approaches zero, f will approach 1. On the other side when the wave number k_s goes to infinity, f goes to 0. The same goes for the Rayleigh and Prandtl number. If one of the numbers increases, f is expected to move towards 0, if the numbers decrease, f is expected to move towards 1. This all is summarized again in Equation 4.3.

$$\begin{array}{llll} f \to 0 & Ra \uparrow & Pr \uparrow & k_s \uparrow \\ f \to 0 & Ra \downarrow & Pr \downarrow & k_s \downarrow \end{array} \tag{4.3}$$

As we see a similar trend with the heat transfer versus stripes, it is not impossible to think that there is a function g, which behaves similar to function f, for the heat transfer. This definitely can be called remarkable as it suggest that with a heavily patterned plate almost the same results can be made as with a homogeneous plate. As this sounds very interesting for various applications in industry, we should look more into this. For now we have only applied the stripes to the top plate. It is not known if the same results apply when the bottom plate is patterned or if both plates have the patterning.

We have learned from the spectral analysis that we can clearly identify the patterning close to the wall. However, when moving away from the border the effects from the patterning disappear rapidly. At z=0.992, which is about half the thermal boundary layer thickness, the pattern can hardly be identified. Moving outside of the boundary layer, the pattern is not visible at all. This indicates that the whole pattern effect is made invisible by the thermal boundary layer. Only in the $f = 1$ simulation we saw a clear large scale effect of the stripe, however this was expected as the flow can only be cooled at the conducting stripe which on its turn makes the fluid move down.

4.3 Insulating checkerboard pattern

4.3.1 Geometry and simulation domain

Now that we have investigated the stripes, we can extend the same pattern in an additional direction. This will result in a pattern which resembles a checkerboard in which equally size square regions are insulating or conducting. Figure 4.16 shows an overview of the geometry.

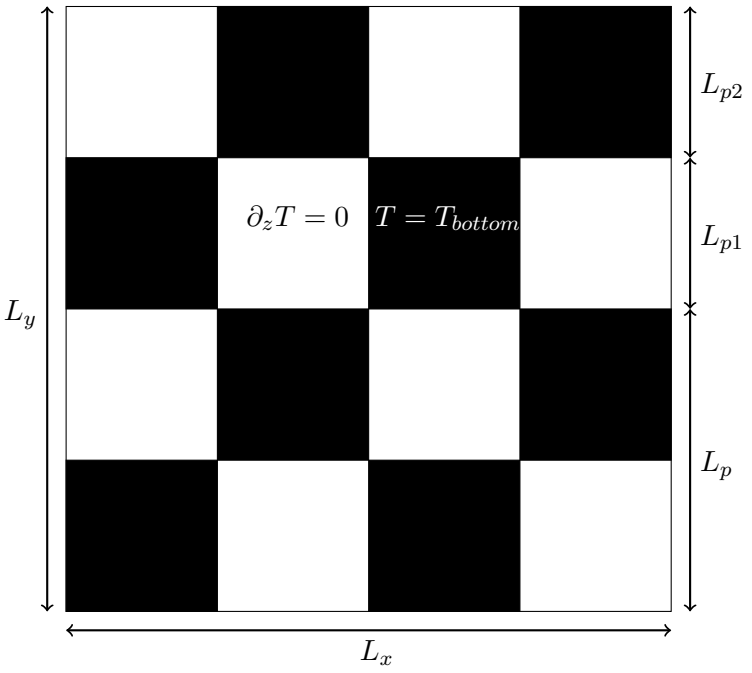

FIGURE 4.16: The checkerboard geometry is identical to the stripe pattern and is extended in the second horizontal dimension. The system still has a single wavelength or frequency and the conducting and insulting area is equal in all simulations.

As with the stripes, this pattern will only be present on the top plate of the system. The periodicity is now in two directions so the equations change only slightly. Again, the adiabatic area is equal to the conducting area, so $L_{p1} = L_{p2} = L_p/2$. All other parameters are an exact match with the stripes simulation.

$$\begin{cases} T(x,y,h) = T_{top} & x,y \in [jL_p, L_{p2} + jL_p], j \in \mathbb{Z} \\ \partial_z T(x,y,z) \mid_{z=h} = 0 & x,y \notin [jL_p, L_{p2} + jL_p], j \in \mathbb{Z} \\ T(x,y,0) = T_{bottom} & \forall x,y \end{cases} \tag{4.4}$$

4.3.2 Flow visualization

Again, to give a feel for flow field, snap shots have been created from the temperature field. These are created from the instantaneous fields with $f = 4$ and $f = 20$ and are shown in Figure 4.17.

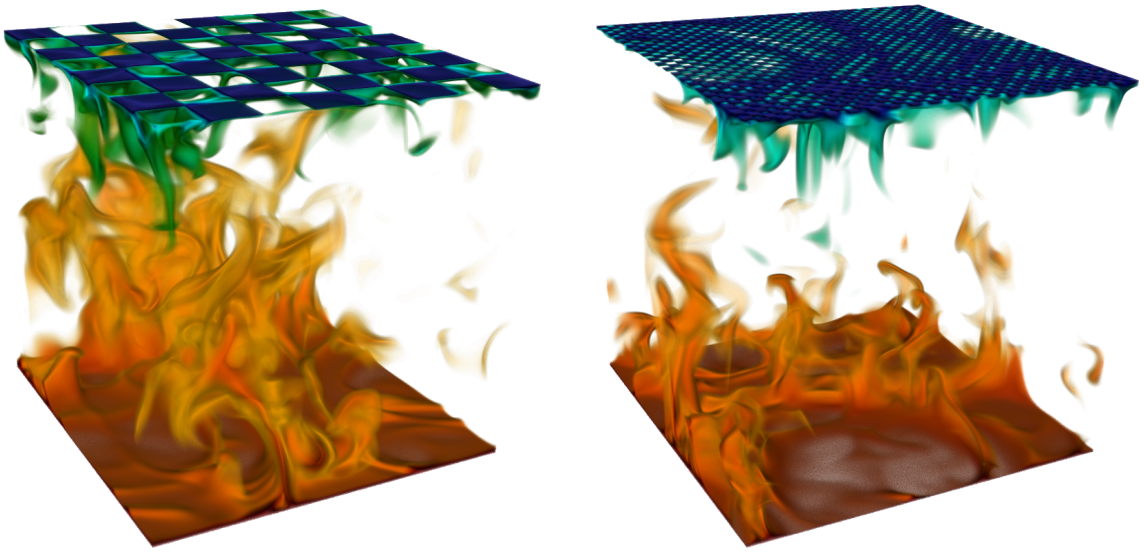

FIGURE 4.17: Snapshot of the instantaneous temperature field for the simulations for $f = 4$ and $f = 20$.

4.3.3 Global quantities

First, we look at the heat transfer of the system and how it compares to the stripe simulation. The results are plotted in Figure 4.18. The first thing to notice is that the error bars are very small when compared to the stripes simulation and these simulations have better statistical convergence.

Another thing that we can see is that the heat transfer from the stripes and the checkerboard simulations are approximately the same. Again, at $f = 1$, the heat transfer is around two thirds of the homogeneous RB. When increasing the wave number it is approaching the homogeneous RB Nusselt number. Also the bulk temperature is almost identical to the stripes simulation. Only the end part of the curve looks more smooth.

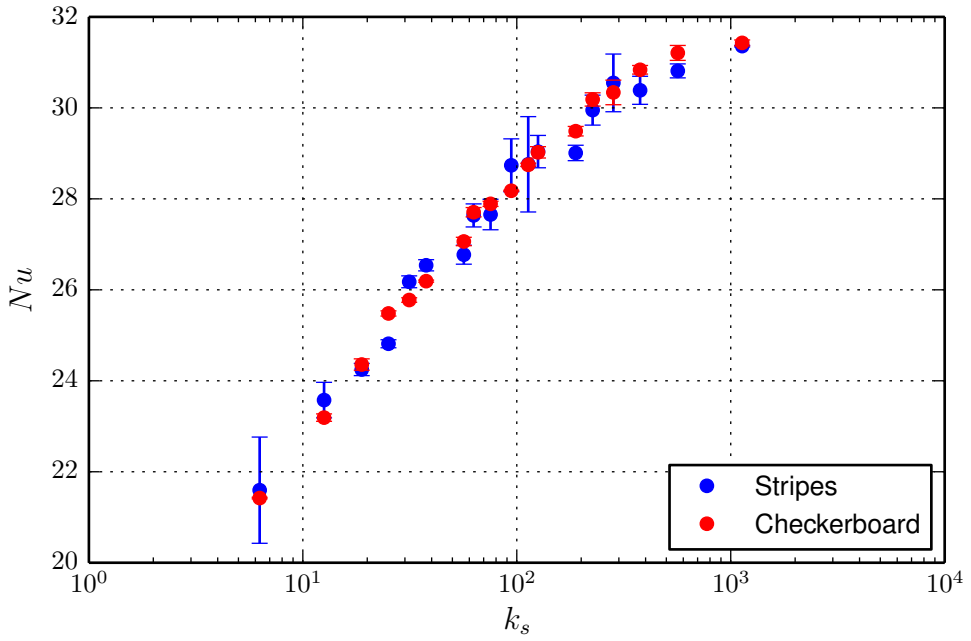

FIGURE 4.18: Wave number versus the Nusselt number. There is not much difference in the Nusselt number between the checkerboard and stripes simulations.

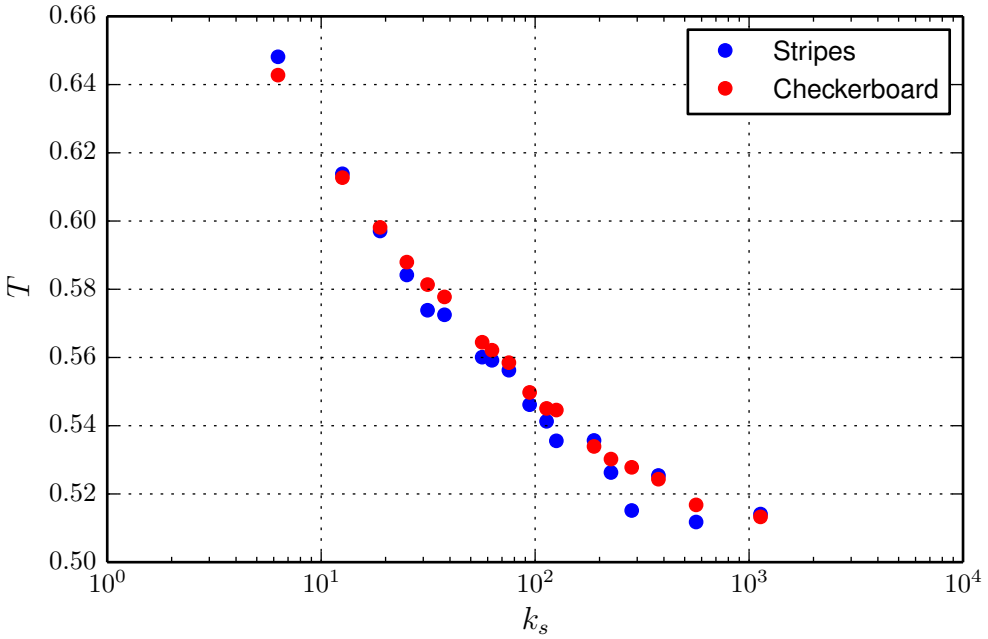

FIGURE 4.19: Wave number versus bulk temperature. Again, the curves almost overlap.

To check how the large scale circulation is oriented with this new pattern, new plots have been created and are shown in Figure 4.20. The average position of the upward plumes is again right under the adiabatic region, however, this time the average position of the downward plumes is also below the adiabatic region. As this seems peculiar another

plot has been made which shows the y-z plane of the vertical velocity at x=0.2. This is plotted in Figure 4.21. Here we see that the system does have a small down flow at the conducting area, but also an upwards flow at the same position which cancel each other out in the middle. Only at the conducting region the flow moves downwards quite rapidly.

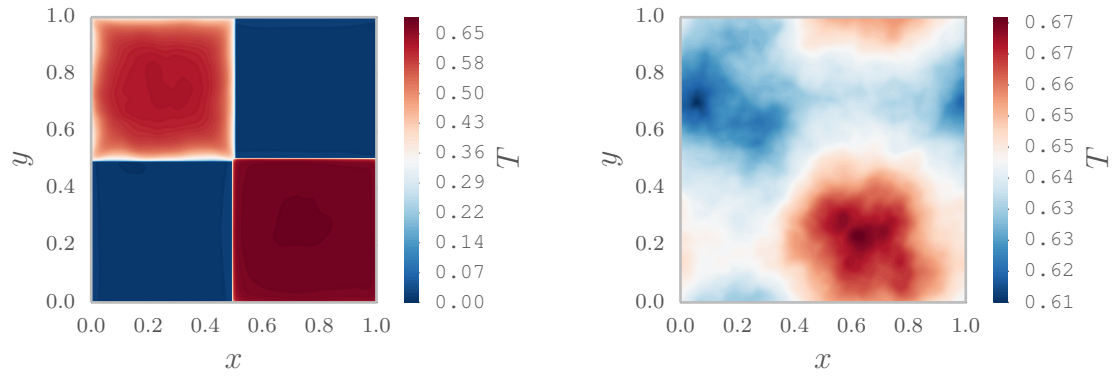

FIGURE 4.20: Left: a time averaged temperature slab, exactly at the border, indicating the blue conducting area and the red insulating area. Right: a time averaged temperature slab exactly in the middle of the system. The upward flow has again placed itself below the adiabatic area, however, the downward flow is also placed below the adiabatic region.

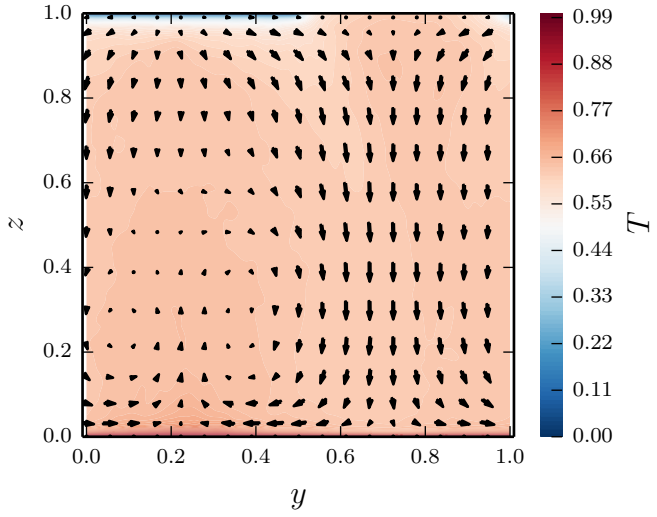

FIGURE 4.21: A time averaged temperature slab at x=0.25. Here we see that the velocity vectors at the top conducting plate are pointing downwards but are opposed by flow moving upwards from the bottom plate. Therefore, the flow is forced to move downwards just below the insulating area, which is remarkable.

4.3.4 Local quantities

When looking at the temperature near the insulating boundary we see small but clear difference with the stripes simulation. The average temperature difference between each point is 0.05. The shape is however identical.

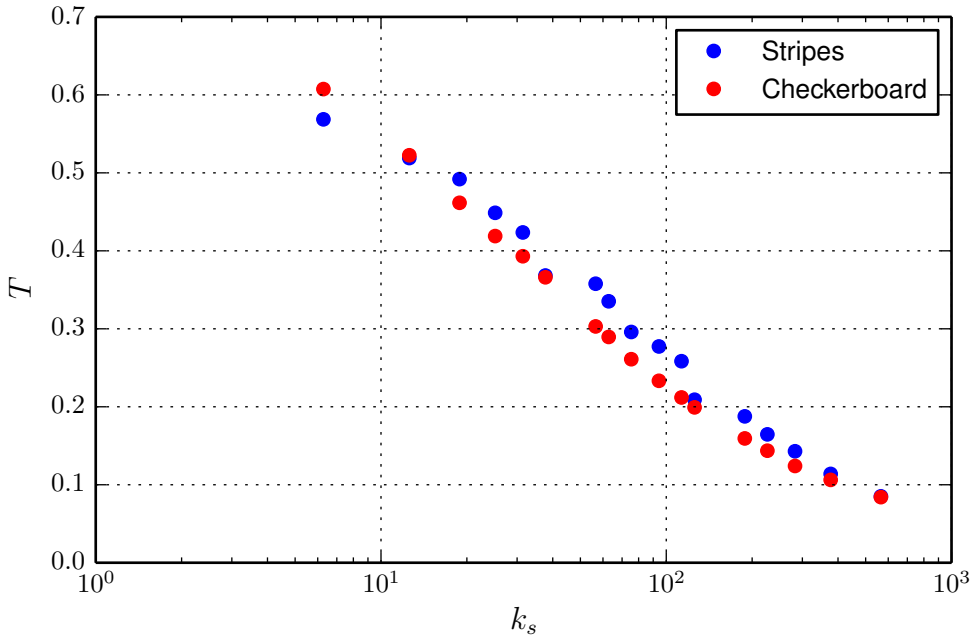

FIGURE 4.22: Wave number versus the temperature at the adiabatic wall. Here a distinct difference is visible between the checkerboard and stripes simulation.

As with the stripes, the temperature profiles near the boundaries have been plotted for various checkerboard frequencies in Figure 4.23. These look very similar to the profiles from the stripe simulations.

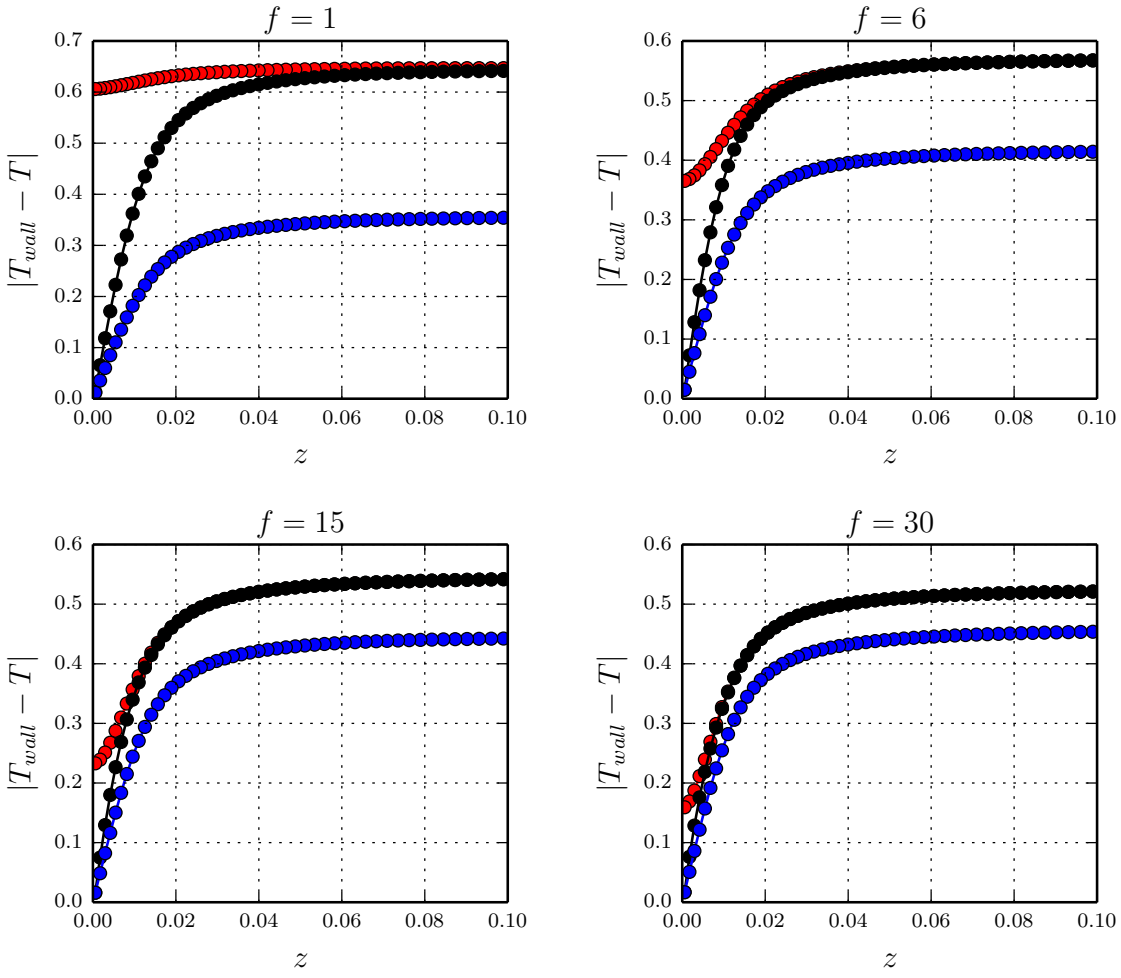

FIGURE 4.23: The average temperature difference from the wall of various checkerboard frequencies. The adiabatic plate area (red dots) and the conducting area (black dots) are plotted as differences from the wall. The bottom plate temperature profile (blue dots) are reversed in temperature, $T(z) = 1 - T(z)$.

4.3.5 Discussion

We have seen that the Nusselt number is the same, within the error bars for the stripes and the checkerboard simulations. One reason for this can be that the total conducting and insulating areas of both systems are identical and therefore, from a global perspective does not change that much. There is only a difference in how these areas are arranged and from these tests it seems that this does not change the global quantities as the Nusselt number that much.

The same is the case for the bulk temperature as this is again almost the same as the stripes simulation. We see a small difference for the extreme case of $f = 1$ and in the tail of the data. A possible explanation could be that the stripes dataset was not statistically converged enough. Still, both quantities are very close and it seems that these global quantities are not influenced by the difference in patterns.

It is quite remarkable that for the lowest frequency, $f = 1$, the large scale circulation organizes the system in such a way that the position of the average downwards flow and

the position of the average upwards flow is always maximized. For the stripes simulation it was possible to place the average downwards flow below the conducting region and the average upwards flow below an insulating region. However, with the checkerboard pattern this is not possible. Still, the system prefers the distance between both flows to be maximized and positions the average downwards flow below the insulating region.

The average temperature just below the insulating region has a small but distinct difference. In the stripes simulations the insulating regions are on average 0.05 hotter than the checkerboard simulations with the same frequency. The total area of the insulating and conducting regions are equal but when looking at the individual patches, the checkerboard pattern is only half the area of the stripe with the same frequency. Also, as the frequency increases, the distance between the conducting and insulating area decreases. With the stripes this is only in one dimension while with the checkerboard this is in two dimensions. This might also possibly be an explanation of the slightly lower temperature.

The temperature profiles also give an interesting overview. We know from homogeneous RB that the temperature profiles are symmetric, meaning that if we would also reverse one of the profiles with the same method as in Figure 4.23 we would have two overlapping lines. As we increase the frequency we see that conducting and insulating curves slowly merge into a single line, with only a small difference very close to the wall. Also the bulk temperature is lowering as all lines slowly move towards a 0.5 temperature.

4.4 Conclusions

In this final chapter, we looked at mixed insulating and conducting boundary conditions. By changing the distribution of both areas, but keeping the area equal, we studied the global and local flow quantities. These distributions are produced by 1D striped patterns and 2D checkerboard patterns.

When comparing the stripe pattern with the checkerboard pattern, we do not see a significant difference in heat transfer. At the lowest k we see a decreased Nu to around 2/3 of the homogeneous case. When we increase k, we see an increase in Nu for both, the stripes and the checkerboard simulations. It is however remarkable that this heat transfer increases to almost the homogeneous case for the last k. The same trend is also visual from the bulk temperature, where it also seems to converge to the homogeneous case for increasing k. The only difference between the stripes and checker simulation is the temperature below the adiabatic region which are on average 0.05 hotter for the stripes simulation.

In the Fourier spectra, we could observe the frequency of the adiabatic pattern close to the top wall boundary. When moving away from the wall, the lines of the spectra started to merge. Almost outside of the thermal boundary layer, these structures were unrecognizable. This implies that these structures are not seen in the LSC.

CHAPTER 5

Summary and outlook

5.1 Summary

In this thesis, the main focus was to study the effect of different boundary variations on flow quantities in Rayleigh-Bénard convection. This was done numerically, using a parallel finite difference solver. Most simulations used $Ra = 10^8$ and $Pr = 1$, however, some simulations also used $Ra = 10^6$ and/or $Pr = 10$.

In the first chapter, small areas with locally larger temperatures, called hot spots, were used to simulate roughness elements on the boundary walls. These elements could possibly position or influence the large scale circulation. Various spot configurations have been tested, but none have shown any significant or reproducible effect on the bulk circulation. We could also not observe any influence from these spots on the thermal boundary layer. In the extreme case, where the system only consists of a hot- and cold spot, keeping the rest of the boundaries at the average bulk temperature, we see a perfectly aligned large scale circulation positioned between the spots. Reducing the temperature difference between the boundary and its corresponding spot, we found the onset of the decoupling at a temperature difference of 0.2.

The next chapter replaced the hot spots by physical roughness. These element differ in dimensions but had a maximum height of 0.05, which is slightly more than twice the height of the thermal boundary layer thickness. Again, no influence on the bulk circulation was observed. Furthermore, 1D and 2D periodic sinusoidal patterns are used on the bottom wall boundary. With increasing f of the sinusoidal structures, Nu for both systems increases until an optimum. After the optimum, Nu, decreases again with increasing f. It is suspected that the flow can take advantage of the additional area for lower f, while for higher f, the cavities between the waves restrict the flow to effectively use the additional space. When compensating the Nu for the additional area, the optimum disappears and both the 1D and 2D patterns decrease rapidly after $f = 6$. The temperature difference from both walls were almost equal at $f = 1$. Increasing f, we saw an increase in difference from both profiles. At $f = 36$, this difference seemed to reduce again. This is however not perfectly clear. We have also done preliminary simulations on 1D triangle waves. There seemed to be no significant difference with the sinusoidal waves.

In the final chapter we studied the distribution of equally sized conducting and insulating areas on the top wall boundary and their effect on the flow quantities. The two areas were divided in stripes or checkerboard patterns. When dividing both areas only in two segments for the stripes, or four segments for the checkerboard, Nu is approximately 2/3 of the homogeneous case. However, by maximizing the number of segments in both cases,

Nu raises to almost the complete homogeneous case. In a spectral analysis, we showed that the distribution of these areas perfectly visible close to the wall boundary. However, moving outside of the thermal boundary layer these structures are indistinguishable.

5.2 Outlook

For the sinusoidal geometries, we have only explored $Ra = 10^8$. At this Ra we observed that the system could make use of the additional area until a certain f, at which secondary circulations were visible between the cavities. By increasing the Ra, we could possibly influence this threshold. Also different Pr should be explored to see its effect.

For both, the 1D and 2D sinusoidal patterns, we observed that the temperature profiles of the top and bottom plate are approximately equal for $f = 1$. Increasing f, we saw the profiles slightly move apart. At $f = 36$ it seems that the profiles are moving closer again. To proof this is actually happening, we need to extend the simulations with higher f.

We have only looked briefly at the triangle wave and have only compare some global quantities to the sinusoidal waves. However, it would be interesting to look at the flow field close to the tips of these triangles, e.g. creating a time series of the velocity field around such a tip. Also, the effect of such a geometry with higher Ra should be explored.

In the study on the mixed insulating and conducting boundary conditions we have only focused on $Ra = 10^8$ and changing the distribution with the wave number k. With this we are only able to see k influences on the heat transfer. Extending the simulations to higher Ra and other Pr will give a more complete picture on the topic. We have observed that maximizing the number of segments, we are getting very close to the homogeneous RB result. As we have only half of the effective area on the top plate makes this very remarkable. By applying the same pattern on both the top and bottom plate, it is unclear whether we would still be close to the homogeneous case.

Acknowledgments

First of all, I want to thank my daily supervisor Rodolfo Ostilla Mónico. In the turbulence course, you have aroused my interest for numerics and it needed not a lot of persuasion to have me started with your Masters project. Your knowledge of computational methods, turbulence, and Rayleigh-Bénard convection seems infinite and you have seen all of my pitfalls or struggles at least once. I am very grateful for all your help, as it even continued unabated when you were so close to your own deadline for your doctoral thesis. The only thing I regret is that we never went diving together. This is probably one of the few things where I can lecture you a bit. I also would like to thank Erwin van der Poel. You and Rodolfo are the numerics experts from the group and it was a privilege to collaborate with both of you. More than once have you helped me solve problems as your door was always open.

Next, I would like to thank Chao Sun and Jeroen Verschuur, for being in my graduation committee. I hope you enjoyed reading my thesis and that this work shows my interest for research in general. Also, I am thankful to professor Detlef Lohse for giving me the possibility to graduate in the Physics of Fluids group. I learned a lot in our meetings.

Furthermore, I would like to thank Roberto Verzicco for his insight in the topic. Even with the great distance between us you could have a helping discussion through the teleconferences. I am also indebted to Luca Biferale for his review on my results.

Also I would like to thank Jacco Snoeijer for his motivating lectures in fluid mechanics. Through these lectures I came to the Physics of Fluids group, a choice which I have never regretted.

Without the flexibility of my employer, it would not have been possible to do this master. Therefore, I am very thankful for Micronit Microfluidics B.V. for giving me the trust and flexibility throughout the last three years. Especially, Wilfred Buesink for his understanding and planning around my university schedule, but also a big thanks for all my other colleagues who more than once have found me not present.

As easy as the bachelor Engineering Physics was at Saxion, as hard as I had to work for this master. Therefore, I cannot forget to thank Matthijs Neut and Martin Klein Schaarsberg. With both of you, I shared several courses. Your clever ideas helped me solve problems more than once. Our talks about our latest CrossFit achievements always kept us longer at the coffee machine as first intended.

Working in the master students room was always very enjoyable. In between the work, discussions, the smell of coffee, or a guitar tune filled the room. The pecking order was not always clear, especially for the so called “feut”. Thanks Rodrigo, for letting me join the night- and weekend shifts.

Over the last three years, times were not always easy, but I got lots of help and understanding from my friends. As times were tough, a pep talk from Floris always kept me going. When I forgot that there were other things in life than work, Floris,

Petra, Rachel, Robin, Wouter, Sabrine, Arnoud, Elise, René, Gijsbert, and Anneke showed me were the party was. I am very grateful for friends like you.

My loving parents never stopped supporting me. Although I changed my goal multiple times, you always kept believing in me. I also would like to thank my loving grandma Hanny, for making the delicious dinners and the supportive talks. Furthermore, I would give thanks to my soon to be parents in law for their understanding and support. As they have followed my progress to the years, I also want to thank Ingrid and Gerard for their support.

Last but not least, I would like to thank my understanding fiancé, Kim. Not only did you support me in the choices I have made, but you have also been a huge help in getting were I am now. Times were not always easy but we both kept believing in our success. I love you with all my heart.

Bibliography

[1] H. Bénard. Les tourbillons cellulaires dans une nappe liquide. *Rev. Gén. Sci. Pur. Appl.*, 11:1261, 1900.

[2] Lord Rayleigh. On convection currents in a horizontal layer of fluid, when the higher temperature is on the under side. *Phil. Mag.*, 32:529–546, 1916.

[3] P. K. Kundu, I. M. Cohen, and D. R Dowling. *Fluid Mechanics, Fifth Edition.* Academic Press, 5 edition, 9 2011.

[4] R. Verzicco and P. Orlandi. A finite-difference scheme for three-dimensional incompressible flows in cylindrical coordinates. *Journal of Computational Physics*, 123(2):402–414, 1996.

[5] E. A. Fadlun, R. Verzicco, P. Orlandi, and J. Mohd-Yusof. Combined immersed-boundary finite-difference methods for three-dimensional complex flow simulations. *Journal of Computational Physics*, 161(1):35–60, 2000.

[6] B. I. Shraiman and E. D. Siggia. Heat transport in high-Rayleigh number convection. *Phys. Rev. A*, 42:3650–3653, 1990.

[7] F. Chillà and J. Schumacher. New perspectives in turbulent Rayleigh-Bénard convection. *The European Physical Journal E: Soft Matter and Biological Physics*, 35(7):1–25, 2012.

[8] G. Ahlers, S. Grossmann, and D. Lohse. Heat transfer and large scale dynamics in turbulent Rayleigh-Bénard convection. *Rev. Mod. Phys.*, 81:503, 2009.

[9] X. L. Qiu and P. Tong. Large scale velocity structures in turbulent thermal convection. *Phys. Rev. E*, 64:036304, 2001.

[10] G. Stringano and R. Verzicco. Mean flow structure in thermal convection in a cylindrical cell of aspect-ratio one half. *J. Fluid Mech.*, 548:1–16, 2006.

[11] E. Brown and G. Ahlers. Large-scale circulation model for turbulent Rayleigh-Bénard convection. *Phys. Rev. Lett.*, 98:134501, 2007.

[12] G. Freund, W. Pesch, and W. Zimmermann. Rayleigh–Bénard convection in the presence of spatial temperature modulations. *Journal of Fluid Mechanics*, 673: 318–348, 2011.

[13] G. Stringano, G. Pascazio, and R. Verzicco. Turbulent thermal convection over grooved plates. *J. Fluid Mech.*, 557:307–336, 2006.

[14] Y. B. Du and P. Tong. Enhanced heat transport in turbulent convection over a rough surface. *Phys. Rev. Lett.*, 81:987–990, 1998.

[15] Y. B. Du and P. Tong. Turbulent thermal convection in a cell with ordered rough boundaries. *J. Fluid Mech.*, 407:57–84, 2000.

[16] S. Marcq and J. Weiss. Influence of sea ice lead-width distribution on turbulent heat transfer between the ocean and the atmosphere. *The Cryosphere*, 6:143–156, 2012.

[17] P. Ripesi, L. Biferale, M. Sbragaglia, and A. Wirth. Natural convection with mixed insulating and conducting boundary conditions: low-and high-Rayleigh-number regimes. *Journal of Fluid Mechanics*, 742:636–663, 2014.